

Entry Guidance: A Unified Method

Ping Lu*

Iowa State University, Ames, Iowa 50011-2271

DOI: 10.2514/1.62605

During the past five decades, entry guidance methods have gone through major evolutions, largely driven by the needs of different types of entry vehicles and greatly increased onboard computation capabilities. Numerical predictor-corrector algorithms have emerged in recent years to hold the potential to become the next prevalent entry guidance method. This paper aims at developing a method that is centered on a single baseline predictor-corrector algorithm and will be applicable to a wide range of vehicles with varying lifting capabilities for orbital as well as suborbital entry missions. Different needs for additional (vehicle- and mission-dependent) trajectory shaping and inequality constraint enforcement are met by appropriate augmentations of altitude-rate feedback to the baseline algorithm. In particular, the long-standing challenge of enforcing common inequality trajectory constraints (such as the heating rate and load factor) with a predictor-corrector algorithm is now satisfactorily overcome, for either low-lifting or high-lifting vehicles. The method is successfully applied to three very different vehicles, a capsule, a shuttle-class vehicle, and a high-lifting hypersonic gliding vehicle.

I. Introduction

ENTRY guidance in aerospace engineering refers to the onboard process in which the steering commands for a hypersonic vehicle with aerodynamic lifting capability are generated, so as to guide the vehicle from its initial condition to safely and accurately reach the specified final condition. Although the physical principle of entry guidance remains, in essence, the same (i.e., the carefully controlled dissipation of energy in accordance with the ranging requirement and other trajectory constraints), the specific guidance methods are different, depending on the types of vehicles. Historically, entry guidance algorithms have seen the evolution of three major generations. The first-generation entry guidance algorithm was designed for low-lifting capsule vehicles in the Apollo program [1,2]. The Apollo entry guidance algorithm actually consists of two distinct parts, one for a skip entry phase and the other for a final entry (or direct entry) phase, even though it is the latter that is customarily called the Apollo entry guidance algorithm. In either phase, the Apollo vehicle flies the trim angle of attack without modulation. The Apollo direct entry guidance algorithm uses adjoint variables as the sensitivity coefficients for the predicted downrange error with respect to trajectory dispersions. The adjoint variables are obtained from the linearized trajectory dynamics around a given reference trajectory. The guidance command for the bank angle is generated to null this predicted downrange error. Even though the guidance algorithm does not explicitly track the reference trajectory, the working principle heavily depends on the reference trajectory to generate the sensitivity coefficients and compute trajectory dispersions. The sign of the bank angle is determined by a bank-angle reversal logic that changes the sign to the opposite whenever the crossrange to the landing site exceeds a velocity-dependent deadband. Realizing the inevitable and probably large dispersions in the initial condition of the skip phase when skip entry is to be performed, Apollo skip entry guidance takes a completely different approach. A skip trajectory is designed onboard based on the actual initial condition during the early part of the skip entry. This trajectory is then tracked by a linearized feedback tracking law that in turn produces the guidance command for the magnitude of the bank angle. To reduce the

computational requirements of the skip entry guidance algorithm within the capability of the Apollo Guidance Computer (which is unbelievably meager by today's standards), the algorithm has to rely mostly on analytical, approximate, and empirical relationships. These limitations adversely affect the precision and applicability of the Apollo skip entry guidance algorithm in missions with even just moderately long downranges [3–7].

The space shuttle entry guidance algorithm represents the second-generation entry guidance technology [8,9]. As an entry vehicle, the shuttle has a considerably higher lift-to-drag (L/D) ratio than the Apollo Command Module (CM). Consequently, the flight time and downrange traveled by the shuttle are much longer. Another major difference is that the shuttle lands horizontally; hence, the entry phase terminates at a supersonic speed of Mach 2.5 and 60 n miles before the landing site. Unlike the Apollo CM, the flight-path angle of the shuttle remains small throughout the entry flight. In the guidance algorithm, a reference longitudinal trajectory is defined by a drag acceleration vs Earth-relative velocity profile for high Mach numbers and a drag-vs-energy profile for lower Mach numbers. It can be shown that, when the curvature of the ground track of the trajectory is ignored and the flight-path angle is small, the drag profile(s) will determine the downrange the vehicle can achieve. A linearized, gain-scheduled tracking law for bank-angle magnitude modulation is then employed to follow the reference drag profile, providing the commanded bank-angle magnitude. A bank-reversal logic similar to that in the Apollo entry guidance is used to determine the sign of the bank-angle command. The nominal angle-of-attack profile is prescribed based on thermal-protection, trim-flight, and crossrange considerations. However, the angle of attack is also modulated within a few degrees from the nominal profile for tighter tracking performance, especially during bank reversals. In addition, an early version of an adaptive feature is built in the algorithm to allow minor onboard adjustments of the reference drag profile to null the accumulated range error due to trajectory dispersions.

Various improvements to the shuttle's acceleration-based entry guidance method have been proposed over the years. These efforts seek to simplify or automate the design of the reference drag profile, improve the accuracy of the drag profile [10–12], investigate nonlinear and linear full-state feedback tracking laws [13–17], or improve on both reference trajectory design and tracking control [18–20]. By and large, these efforts are still within the confines of the basic shuttle entry guidance method.

The third-generation entry guidance algorithms share two common traits (aside from the fact that a majority of them have appeared in recent years): they depart from the Apollo or shuttle entry guidance method, and they rely much more on onboard computation for a real-time trajectory design and guidance solution. The algorithms in [21] and [22] use the so-called quasi-equilibrium glide

Received 27 March 2013; revision received 25 July 2013; accepted for publication 25 July 2013; published online 19 February 2014. Copyright © 2013 by Ping Lu. Published by the American Institute of Aeronautics and Astronautics, Inc., with permission. Copies of this paper may be made for personal or internal use, on condition that the copier pay the \$10.00 per-copy fee to the Copyright Clearance Center, Inc., 222 Rosewood Drive, Danvers, MA 01923; include the code 1533-3884/14 and \$10.00 in correspondence with the CCC.

*Professor, Department of Aerospace Engineering, 2271 Howe Hall; plu@iastate.edu. Associate Fellow AIAA.

condition (QEGC), a frequently observed phenomenon in the hypersonic lifting flight of vehicles with moderate and higher L/D ratios, as the foundation for the rapid online design of a feasible entry trajectory subject to typical inequality path constraints. An adaptive lateral guidance logic for determining when to perform bank-angle reversals for ensured performance in the most stressful scenarios is investigated in [23]. The work in [24] uses an online numerical integration to search for guidance parameters in order to design a feasible trajectory. The results of a battery of very rigorous and stressful tests of the entry guidance algorithms in [17,20,21,22, and 24] with the shuttle entry guidance algorithm [8] as a baseline are reported in [25].

Among the third-generation entry guidance algorithms, the class of predictor-corrector algorithms has evolved and emerged to show great potential [3–6,26–32]. The most notable strengths of these methods include the capability to adapt to large trajectory dispersions, no reliance on a preplanned reference trajectory, and no need for a separate trajectory planner and tracking law. Most of these algorithms are still relatively simple and computationally viable for onboard implementation. Strong evidence has been reported on the clear superiority of these algorithms over the Apollo skip entry guidance algorithm in skip entry missions [3–6]. However, compared to entry guidance algorithms based on tracking a reference such as the shuttle algorithm [8], a long-standing weakness of the predictor-corrector guidance algorithm has been the lack of effective and broadly applicable means to enforce inequality trajectory constraints such as those on the heating rate and aerodynamic load. This may have been a reason why predictor-corrector entry guidance algorithms have largely been proposed for low-lifting entry vehicles for which the satisfaction of these constraints is mainly through a carefully controlled initial condition. But this issue was begun to be addressed recently in [31], in which the QEGC is employed to enforce common inequality entry trajectory constraints in the numerical process of a predictor-corrector algorithm. Another issue is the convergence of the numerical process. For onboard convergence robustness, the most reliable algorithms today all iterate on one single guidance parameter. In certain applications such as aerocapture [26], however, the limitation to one degree of freedom in guidance design may be too restrictive to achieve all desired characteristics of the trajectory.

The current state of entry guidance algorithms is thus a fragmented one. For entry flight of vehicles with medium to higher L/D ratios, the shuttle approach is still prevalent. For low-lifting vehicles, the predictor-corrector algorithm becomes a popular choice. Complicating the matter further, the trajectory characteristics of suborbital entry, often dramatically different from those in orbital entry (e.g., with a positive initial flight-path angle), require different logic and significant additional patches in the guidance algorithm [22,24,33]. With the strong recent interest in suborbital hypersonic gliding flight [32], suborbital entry guidance will only become a more frequent need.

With all the research and development in entry guidance algorithms, most notably in recent years, it is the contention of this paper that the practitioners in the community would benefit from a unified entry guidance method. By unified method, it is meant to be based on the same algorithmic principle(s), with a common set of options that will be applicable to a wide range of possible vehicle configurations, whether with low or high L/D ratios, and to orbital entry (including skip entry) and suborbital entry missions alike. Such a method should be able to effectively respond to the different situations intended to be covered but requires no mission-dependent and few, if any, vehicle-dependent adjustments. The algorithm should be relatively simple and highly robust. Equally importantly, the method must have a technically sound, readily implementable, and widely applicable mechanism to enforce common inequality entry trajectory constraints while still ensuring the guidance performance (precision) for low- and high-lifting entry vehicles.

In this paper, such a unified entry guidance method is proposed, which uses a numerical predictor-corrector algorithm as the baseline algorithm. This algorithm relies only on the basic working principle of entry guidance, the use of the bank angle to control the vertical

component of the aerodynamic lift, not on any vehicle- or trajectory-specific characteristics. Although the basic idea of the the baseline algorithm is similar to a design investigated in [30] and [4], the improved formulation, new stopping criteria, and convergence discussion offer more insight into the approach. The unified method is an augmented predictor-corrector entry guidance that is this baseline algorithm, augmented by objective-oriented altitude-rate feedback compensations. When augmented with an altitude-rate compensation required for the equilibrium glide, the guidance system would effectively eliminate large phugoid trajectory oscillations of high L/D ratio vehicles, provide a reliably smooth transition between the initial descent and near-equilibrium glide for medium L/D ratio vehicles in orbital entry missions, and significantly reduce the peak heating rate and load factor for medium to high L/D ratio vehicles. When reliable enforcement of the inequality trajectory constraints is required, the altitude-rate augmentation term is obtained on the basis of the natural time-scale separation of the trajectory dynamics and a nonlinear predictive control technique. It is shown that such an approach provides effective and accurate predictive load relief for capsule vehicles while still ensuring guidance precision in all feasible cases, something that has long been desired but never achieved until now. For medium to high L/D ratio vehicles, a similarly augmented predictor-corrector guidance will reliably and accurately enforce the heating-rate and load factor inequality constraints by actively shaping the trajectory while maintaining high guidance precision.

The proposed algorithm is demonstrated by applications to three very different vehicles: a capsule with a L/D ratio less than 1/3 of that of the shuttle, a lifting body with a L/D ratio comparable to that of the shuttle, and a hypersonic gliding vehicle with a L/D ratio that is more than 3 times that of the shuttle. Both orbital and suborbital missions are examined.

II. Preliminary

The three-dimensional equations of motion of a gliding vehicle over a spherical, rotating Earth in terms of nondimensional variables are

$$\dot{r} = V \sin \gamma \quad (1)$$

$$\dot{\theta} = \frac{V \cos \gamma \sin \psi}{r \cos \phi} \quad (2)$$

$$\dot{\phi} = \frac{V \cos \gamma \cos \psi}{r} \quad (3)$$

$$\begin{aligned} \dot{V} = & -D - \left(\frac{\sin \gamma}{r^2} \right) \\ & + \Omega^2 r \cos \phi (\sin \gamma \cos \phi - \cos \gamma \sin \phi \cos \psi) \end{aligned} \quad (4)$$

$$\begin{aligned} \dot{\gamma} = & \frac{1}{V} \left[L \cos \sigma + \left(V^2 - \frac{1}{r} \right) \left(\frac{\cos \gamma}{r} \right) + 2\Omega V \cos \phi \sin \psi \right. \\ & \left. + \Omega^2 r \cos \phi (\cos \gamma \cos \phi + \sin \gamma \cos \psi \sin \phi) \right] \end{aligned} \quad (5)$$

$$\begin{aligned} \dot{\psi} = & \frac{1}{V} \left[\frac{L \sin \sigma}{\cos \gamma} + \frac{V^2}{r} \cos \gamma \sin \psi \tan \phi \right. \\ & - 2\Omega V (\tan \gamma \cos \psi \cos \phi - \sin \phi) \\ & \left. + \frac{\Omega^2 r}{\cos \gamma} \sin \psi \sin \phi \cos \phi \right] \end{aligned} \quad (6)$$

where r is the radial distance from the Earth center to the vehicle, θ and ϕ are the longitude and latitude, V is the Earth-relative velocity, γ

the is flight-path angle of the Earth-relative velocity vector, and ψ is the heading angle of the same velocity vector, measured clockwise in the local horizontal plane from the north. In dimensionless form, length is normalized by the equatorial radius of the Earth $R_0 = 6,378,135$ m, and time is normalized by $t_{\text{scale}} = \sqrt{R_0/g_0}$, where $g_0 = 9.81$ m/s². The choices of the distance and time normalization lead to the velocity being normalized by $V_{\text{scale}} = \sqrt{g_0 R_0}$. The differentiations in the previous equations are with respect to the dimensionless time $\tau = t/t_{\text{scale}}$. The terms L and D are the nondimensional aerodynamic lift and drag acceleration (in g_0), respectively. The bank angle σ is the roll angle of the vehicle about the relative velocity vector, positive to the right. Note that the bank angle is not the same as the body roll angle whenever the angle of attack is not zero. Finally, Ω is the (dimensionless) Earth self-rotation rate. Since the time is not a critical parameter in this problem, an energylike variable e will be used as the independent variable in guidance algorithm development:

$$e = \frac{1}{r} - \frac{V^2}{2} \quad (7)$$

It is clear that e , defined in Eq. (7), is the negative of the specific mechanical energy used in orbital mechanics. If the Earth-rotation term in Eq. (4) is ignored, it can be readily shown that

$$\frac{de}{d\tau} = DV > 0 \quad (8)$$

Therefore, e is a monotonically increasing variable. Let $\mathbf{x} = (r \ \theta \ \phi \ \gamma \ \psi)^T$ be the reduced-order state vector, whereas the velocity V is determined by $V = \sqrt{2(1/r - e)}$. The angle of attack α enters in L and D through the dependence on α by the lift and drag coefficients C_L and C_D .

As in most entry guidance developments, the angle-of-attack profile is considered to be fixed as a given function of the Mach number or relative velocity. This profile is determined by considerations in ranging capability (in the downrange and/or crossrange direction), thermal protection, and flight control. However, the guidance algorithm to be developed is independent of any particular angle-of-attack profile.

The trajectory control is the bank angle σ , which is to be determined by the guidance algorithm. The full three-degree-of-freedom (3DOF) equations of motion in Eqs. (1–6), excluding Eq. (4), may be rewritten with e as the independent variable:

$$\mathbf{x}' = \frac{d\mathbf{x}}{de} = \mathbf{f}(\mathbf{x}, \sigma), \quad \mathbf{x}(e_0) = \mathbf{x}_0 \quad (9)$$

The initial condition of the system in Eq. (9) is taken to be the current state \mathbf{x}_0 at the current energy e_0 . The typical final constraints are that the trajectory reaches a position at a specified distance s_f^* (s_f^* can be zero) from the target location at a specified final altitude r_f^* and velocity V_f^* . In other words,

$$r(\tau_f) = r_f^* \quad (10)$$

$$V(\tau_f) = V_f^* \quad (11)$$

$$s(\tau_f) = s_f^* \quad (12)$$

where s denotes the great-circle range to the landing site, normalized by R_0 (hence, s is in radians), and it is a function of longitude and latitude. The specified final range-to-landing site $s_f^* \geq 0$ is typically tens of nautical miles for horizontal landing, while $s_f^* = 0$ for vertical landing. The first two conditions in Eqs. (10) and (11) may be combined to define a specified final energy $e_f = 1/r_f^* - V_f^{*2}/2$. Thus, the single terminal constraint is

$$s(e_f) = s_f^* \quad (13)$$

For entry flight, $1.0 \leq r \leq 1.0188$. Hence, the variation in e comes predominantly from the variation in the kinetic energy term $V^2/2$. Therefore, at $e_f = 1/r_f^* - V_f^{*2}/2$ the condition $V_f = V_f^*$ is satisfied accurately. The final r_f may differ from r_f^* by a small amount, which in many applications is acceptable.

The typical entry trajectory inequality path constraints include those on heating rate \dot{Q} , load factor a , and dynamic pressure \bar{q} :

$$\dot{Q} = k_Q \sqrt{\rho} V^{3.15} \leq \dot{Q}_{\max} \quad (14)$$

$$a = \sqrt{L^2 + D^2} \leq a_{\max} \quad (15)$$

$$\bar{q} = (g_0 R_0 \rho V^2)/2 \leq \bar{q}_{\max} \quad (16)$$

where Eq. (14) is the heating rate (in watts per square meter) at a stagnation point on the surface of the vehicle with a curvature radius of 0.3048 m (1 ft), and $k_Q = 9.4369 \times 10^{-5} \times (\sqrt{g_0 R_0})^{3.15}$. Note that in Eqs. (14) and (16), V is nondimensional as defined before, but the atmospheric density ρ has the unit of kilograms per cubic meter. The heating-rate limit is \dot{Q}_{\max} in watts per square meter, the load factor limit is a_{\max} in g , and the dynamic-pressure limit is \bar{q}_{\max} in newtons per square meter.

The problem of entry guidance is to find the bank-angle command at each instant, based on the current state, so that the corresponding trajectory of the system in Eq. (9) will satisfy the boundary conditions [on $\mathbf{x}(e_0)$ and Eq. (13)] as well as the path constraints in Eqs. (14–16). The trajectory inequality constraints in Eqs. (14–16) will not be included in the baseline algorithm in the next section, but they will be enforced in the final algorithm in Sec. VI.

III. Baseline Predictor-Corrector Guidance Algorithm

Although the basic idea in this section is similar to one of the designs first investigated in [30] and then [4], the improved formulation, new stopping criteria, and convergence discussion in the following offer the assurance of the algorithm for finding a meaningful solution in all cases. The baseline predictor-corrector guidance algorithm determines a complete profile of the bank-angle magnitude and the corresponding feasible longitudinal trajectory from the current condition to the termination of the entry phase. Let s again denote the range to go (in radians) on the surface of a spherical Earth along the great circle connecting the current location of the vehicle and the site of the final destination. When the offset between the azimuth of this great circle and the heading angle is ignored, the differential equation that governs s is

$$\dot{s} = \frac{ds}{d\tau} = -V \cos \gamma / r \quad (17)$$

Let $\mathbf{y} = (r \ \theta \ \phi \ \gamma \ \psi \ s)^T$, and denote the differential Eqs. (1–3), (5), (6), and (17) by

$$\frac{d\mathbf{y}}{de} = \hat{\mathbf{f}}(\mathbf{y}, \sigma, e) \quad (18)$$

where $V = \sqrt{2(1/r - e)}$ is used wherever V is needed. Note that it is essential to include s in Eq. (18), instead of representing the range to go by the great-circle arc length between a point on the trajectory and the landing site, computed by spherical trigonometric functions. The result from the spherical trigonometric functions cannot distinguish an undershoot case from an overshoot case, which will make the convergence of the subsequent algorithm very difficult. Also, unlike in the shuttle entry guidance approach [8], no assumption on the smallness of $|\gamma|$ is required for the rest of the development. Hence, this method is applicable to capsule vehicles for which the entry

trajectories will see a large (negative) flight-path angle γ toward the end.

The bank-angle magnitude profile sought is parameterized by a linear function of e :

$$|\sigma(e)| = \sigma_0 + \frac{e - e_0}{e_f - e_0} (\sigma_f - \sigma_0) \quad (19)$$

where $\sigma_0 \geq 0$ is a parameter to be found, and $\sigma_f > 0$ can be a prescribed constant or set to equal to σ_0 . A discussion on how a sufficiently large σ_f may be selected to increase the robustness of the guidance with respect to large modeling uncertainty for low-lifting vehicles is found in [30]. If $\sigma_f = \sigma_0$ is taken, then the parameterized σ profile is a constant.

Once a σ_0 is specified, the complete bank-angle magnitude profile is defined per Eq. (19). The sign of σ will be determined by the bank-reversal logic to be described later in this section, and an instantaneous change of the sign of σ is used in the guidance solution whenever a bank reversal is called for. In each guidance cycle, the appropriate value of σ_0 is to be solved so that the solution to Eq. (18) leading from the current condition to the final energy e_f , under the bank-angle profile defined in Eq. (19), satisfies the terminal constraint

$$z(\sigma_0) = s(e_f) - s_f^* = 0 \quad (20)$$

The error $z = s(e_f) - s_f^*$ in Eq. (20) can be regarded as a function (albeit implicit) of σ_0 . In most numerical predictor-corrector entry guidance algorithms (including [30]), Eq. (20) is treated as a zero-finding problem. Here, an alternate perspective is taken: find σ_0 to minimize the error function:

$$f(\sigma_0) = \frac{1}{2} z^2(\sigma_0) = \frac{1}{2} [s(e_f) - s_f^*]^2 \quad (21)$$

At the current e_0 and for the k th iterate $\sigma_0^{(k)}$, the predictor step of the algorithm will numerically integrate Eq. (18) from the current state to e_f , using the σ profile with the magnitude given in Eq. (19) and sign determined by the bank-reversal logic. The value of the error function $f(\sigma_0^{(k)})$ is evaluated. If the stopping criterion (to be presented later) is not yet met, the corrector step of the algorithm seeks to update σ_0 by a step-size-controlled Gauss–Newton method,

$$\sigma_0^{(k+1)} = \sigma_0^{(k)} - \lambda_k \frac{\partial f(\sigma_0^{(k)}) / \partial \sigma_0}{[\partial z(\sigma_0^{(k)}) / \partial \sigma_0]^2} \quad (22)$$

where the step-size parameter λ_k is chosen to be $1/2^i$ and i is the smallest integer (including 0) such that $f(\sigma_0^{(k+1)}) < f(\sigma_0^{(k)})$. The partial derivative in Eq. (22) is computed by the finite difference. The predictor-corrector process is repeated until the stationary condition $\partial f / \partial \sigma_0 = 0$ is numerically met,

$$\left| \frac{\partial f(\sigma_0^{(k+1)})}{\partial \sigma_0} \right| = \left| z(\sigma_0^{(k+1)}) \frac{\partial z(\sigma_0^{(k+1)})}{\partial \sigma_0} \right| \leq \varepsilon \quad (23)$$

for a preselected small $\varepsilon > 0$. Note that Eq. (23) is satisfied when either $|z| = |s(e_f) - s_f^*| = 0$ or $f = z^2/2$ reaches its minimum and $\partial z / \partial \sigma_0 = 0$. The latter corresponds to the case of low energy when the vehicle will reach a final condition with smallest $|s(e_f) - s_f^*|$.

A closer examination reveals that the update in Eq. (22) can be simplified to

$$\sigma_0^{(k+1)} = \sigma_0^{(k)} - \lambda_k \frac{z(\sigma_0^{(k)})}{\partial z(\sigma_0^{(k)}) / \partial \sigma_0} \quad (24)$$

This equation is the same as a modified (step-size-controlled) Newton–Raphson method applied to Eq. (20). This is because for a least-squares problem with a single univariate function [as in Eq. (21)], the Gauss–Newton method is exactly the same as the

Newton–Raphson method. An immediate benefit of this realization is the assurance that the Gauss–Newton iteration in Eq. (24) enjoys locally superlinear or quadratic convergence like the Newton–Raphson method does, depending on whether the function $z(\sigma_0)$ is continuously differentiable or the Lipschitz is continuously differentiable [34]. Such strong convergence results are not generally true for the Gauss–Newton method in other cases. If the partial derivative in Eq. (24) is approximated by a secant scheme based on the two consecutive previous iterates, the update becomes

$$\sigma_0^{(k+1)} = \sigma_0^{(k)} - \lambda_k \frac{z(\sigma_0^{(k)})}{[z(\sigma_0^{(k)}) - z(\sigma_0^{(k-1)})]} (\sigma_0^{(k)} - \sigma_0^{(k-1)}) \quad (25)$$

Similar to a secant scheme, the iteration in Eq. (25) enjoys superlinear convergence [34]. These convergence results are not just for pure theoretical satisfaction. They imply the reliable and rapid convergence behavior of the algorithm, which is critical for onboard applications. But, unlike in a root-finding problem, the minimization of $f(\sigma_0)$ in Eq. (21) together with the stopping criterion in Eq. (23) offers a reassurance: even in the case when the terminal constraint in Eq. (20) cannot be met (because of a shortage in energy, for instance), the algorithm will always find a trajectory that ends with the smallest value of $[s(e_f) - s_f^*]^2$. When the energy is low, the algorithm will still behave in a reliable and predictable fashion to achieve convergence.

The fact that Eq. (24) is the same as a modified Newton–Raphson method applied to the root-finding problem in Eq. (20) suggests the same performance of the two approaches [the minimization of f in Eq. (21) and finding the root of z in Eq. (20)] by the Newton–Raphson method], provided that the root-finding problem in Eq. (20) has a solution. When the root-finding problem in Eq. (20) has no solution, the stopping criterion in Eq. (23) ensures that the current algorithm will stop with the minimum of $f = [s(e_f) - s_f^*]^2/2$, where $z = s(e_f) - s_f^* \neq 0$ but $\partial z / \partial \sigma_0 = 0$.

Note that the working principle of the previously mentioned development is independent of the specifics of the vehicle, the aerodynamic properties of the vehicle, or any assumptions of the trajectory characteristics in particular. The algorithm is based on the basic principle of lifting entry guidance, that is, controlling the bank angle to achieve an appropriate vertical component of the aerodynamic lift-force vector commensurate with the energy and range to go. It is this independence of vehicle and trajectory specifics that enables this baseline algorithm to be applicable to a wide range of entry vehicles.

Once σ_0 has been found, the magnitude of the current bank-angle command σ_{cmd} will have the magnitude of σ_0 . The sign of σ_{cmd} will be determined by a bank-reversal logic similar to that used by the Apollo [1] for low-lifting vehicles such as capsules and that used by the shuttle [8] for medium to high L/D ratio vehicles. Define the current heading offset,

$$\delta\psi = \psi - \Psi \quad (26)$$

where Ψ is the azimuth angle at the current location along the great circle connecting the current location and the target location, and ψ is the current actual heading angle. A velocity-dependent deadband $\Delta_{\text{azmth}}(V)$ is designed. As soon as $\Delta_{\text{azmth}}(V)$ increases from one direction and exceeds $\Delta_{\text{azmth}}(V)$, the bank angle is commanded to change its sign to reduce $|\delta\psi|$. An appropriate design of $\Delta_{\text{azmth}}(V)$ should not require too many bank reversals for low-crossrange missions but should still ensure success in large-crossrange missions. The specifics of such a $\Delta_{\text{azmth}}(V)$ will be dependent on the lifting capability of the vehicle and the specified terminal velocity.

In contrast to the formulation in [30], in which only the longitudinal dynamics are used in the predictor-corrector algorithm, the main benefit of using the 3DOF dynamics in Eq. (18) is better accuracy of the predicted trajectory because the effects of the Earth rotation and crossrange on the trajectory are included. For short-range missions and initial conditions comfortably within the vehicle capability envelop, whether to use the longitudinal dynamics or 3DOF dynamics in the trajectory prediction makes little difference.

For missions with initial conditions near the boundary of the vehicle's capability, however, the added accuracy of using the 3DOF dynamics could mean the difference between success and failure.

Finally, as with any model-based algorithm, significant uncertainties in vehicle aerodynamic coefficients C_L and C_D , atmospheric density, and vehicle mass can have a noticeable impact on the performance of the algorithm. Appropriate online corrections based on measured accelerations may be necessary. Since the aforementioned uncertainties collectively affect the lift and drag accelerations L and D , they need not be estimated separately. In [4], two first-order fading-memory filters for L/L^* and D/D^* , where L^* and D^* are the values of the lift and drag acceleration based on the nominal models, prove to be quite useful in long-range entry (skip entry).

IV. Application to Three Vehicles from Low to High L/D Ratios

The baseline predictor-corrector entry guidance algorithm described in the preceding section is applied to the models of three very different vehicles in terms of lifting capability. Figure 1 shows the configurations of the three vehicles. The first is a capsule crew exploration vehicle (CEV) that is an earlier version of what is now known as the Orion Multiple-Purpose Vehicle. It has a base diameter of 5.5 m and mass of 8383 kg. Its hypersonic trim L/D ratio is about 0.28. The second vehicle is the X-33, which has a medium hypersonic L/D ratio of about 0.9. The third vehicle model is a generic high-performance Common Aero Vehicle, dubbed CAV-H [35]. The CAV-H has a high maximum L/D ratio of 3.5 at hypersonic speeds. More detail on the CAV-H model can be found in [35]. In Fig. 2, the maximum L/D ratio of the CAV-H and the corresponding angle-of-attack profile at different Mach numbers (which is used as the nominal α profile for the CAV-H) are plotted. For the CEV, the trim α at hypersonic speeds is about 160 deg and varies between 155 to 168 deg at lower speeds. For the X-33, the nominal α profile is 45 deg when the Mach number is greater than 10 and then gradually decreases to 16 deg at Mach 2.5 (see [21]). These three vehicles should represent the spectrum of entry vehicles that will likely be encountered in the foreseeable future.

The predictor-corrector guidance algorithm presented in the preceding section is applied to the three vehicles in 3DOF simulations. All the simulation results in this paper are closed-loop simulations, in that the guidance algorithm is called at a 1 Hz rate to provide the guidance commands for the bank angle and angle of attack for trajectory simulations. The bank-angle command is computed by the baseline algorithm, with the current state as the initial condition, and the angle-of-attack command comes directly from the nominal/trim α profile. The equations of motion in Eqs. (1–6) and the 1976 U.S. Standard Atmosphere are used in the simulations. The aerodynamic coefficients are given as functions of the angle of attack and Mach number. In addition, the rate and acceleration of the bank angle are limited so that no unrealistically rapid changes in the bank angle are allowed (such as instantaneous bank reversals). For the capsule vehicle, the limits are 20 deg/s and 10 deg/s², respectively, and 10 deg/s and 5 deg/s² for the X-33 and CAV-H, respectively. The performance of the guidance algorithm is not sensitive to these limits.

The entry and specified final conditions for the three vehicles are listed in Table 1. For the CAV-H vehicle, suborbital initial entry conditions for missions at lower altitudes and/or velocities will also be used, and they are summarized in Table 2. The landing-site

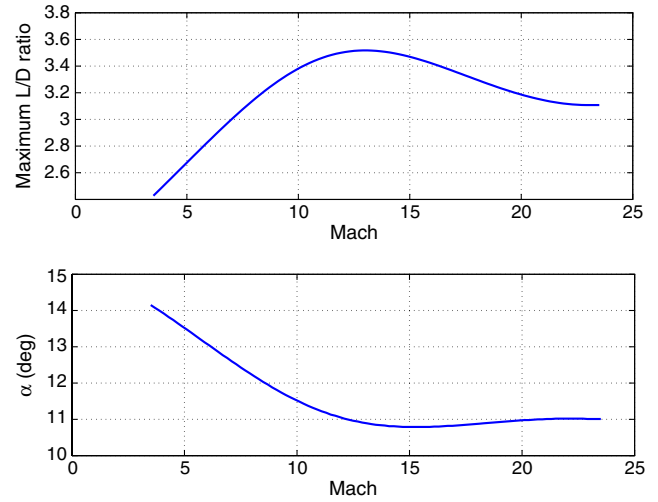


Fig. 2 Maximum hypersonic L/D ratio and corresponding α profile for the CAV-H.

coordinates in terms of longitude and latitude are (279.504 deg, 28.611 deg) (at the Kennedy Space Center) for the X-33 and (242.116 deg, 34.897 deg) (at the Edwards Air Force Base) for the CEV. The destination site coordinates for the CAV-H are (65.7 deg, 31.6 deg).

The predictor-corrector guidance is called every second if the current condition is such that the total aerodynamic acceleration $\sqrt{L^2 + D^2} \geq 1.52 \text{ m/s}^2$ (5 ft/s²); if not, the dynamic pressure is too low for the aerodynamic control to be effective, so the bank-angle command is forced to be the same as the current bank angle. It should be stressed that in all the simulations performed in this paper, no mission-dependent adjustments on the guidance logic or parameters of the baseline algorithm are made, and the only vehicle-dependent adjustments are the deadbands in the bank-reversal logic.

Figure 3 shows the altitude-vs-downrange and altitude-vs-velocity variations along the entry trajectories of the three vehicles for orbital entry missions. The corresponding bank-angle profiles are plotted in Fig. 4. For the CAV-H, its envisioned applications include suborbital entry scenarios. Figure 5 illustrates the three suborbital missions listed in Table 2 for the CAV-H. The range precision at the end of the entry phase is within 1 km for all cases. The baseline predictor-corrector entry guidance algorithm works very well in accurately guiding the trajectory and producing well-behaved bank-angle commands for the three very different vehicles, in orbital entry as well as suborbital entry, all without mission-dependent guidance parameter adjustments.

Although these applications already demonstrate the potential broad applicability of this entry guidance algorithm, certain refinements will still need to be made to ensure a uniformly good quality of the trajectories for all types of vehicles. The entry trajectory for the CEV in Fig. 3 appears perfect. But the trajectories for the CAV-H and X-33 have undesirable phugoid oscillations in the altitude in both Figs. 3 and 5. The higher the L/D ratio of a vehicle is, the more likely these oscillations will occur in the entry trajectory. They are usually not part of the necessary trajectory characteristics for covering the required downrange but a consequence of the lack of coordination between the trajectory control (bank angle in our case)



Fig. 1 Capsule CEV, X-33, and CAV-H lifting-body vehicles.

Table 1 Orbital entry and final conditions for the three vehicles

Vehicle	h_0 , km	V_0 , m/s	s_0 , n mile	h_f^* , km	V_f^* , m/s	s_f^* , n mile
CEV	121.9	7623.5	2035	7.6	150	0
X-33	121.9	7622.0	3528	30.4	908	30
CAV-H	121.9	7400.0	5981	28.0	2000	50

Table 2 Suborbital entry and final conditions for the CAV-H

Mission	h_0 , km	V_0 , m/s	s_0 , n mile	h_f^* , km	V_f^* , m/s	s_f^* , n mile
1	100	7010	5944	28.0	2000	50
2	60	7010	5944	28.0	2000	50
3	50	6400	3993	28.0	2000	50

and changes in the altitude. In the case of the CAV-H, the large phugoid oscillations will produce both cycles of high thermal load and dynamic load stresses. For medium-lifting vehicles such as the X-33, the phugoid oscillations usually appear only in a period right after the initial descent into the dense atmosphere, as can also be seen from Fig. 3. But even this relatively short oscillation can induce a large peak heating rate that exceeds the limit after this transition period. To address this issue, transition strategies have been

investigated in [21] and [31]. They can improve the situation, but the schemes proposed are still too cumbersome and heuristic.

The aforementioned less than satisfying phenomena are not the fault of the baseline guidance algorithm because these considerations are not a part of the design objectives. Incorporating these considerations directly in the baseline algorithm, however, will significantly complicate the algorithm and adversely affect the robustness and convergence of the algorithm. In this paper, a very simple and highly effective approach is taken, and it is the focus of the next section.

The performance of the baseline entry guidance algorithm has been extensively tested and reported in the literature, including applications in skip as well as direct entry, for both capsule and lifting-body vehicles [4,5,30,31]. Therefore, Monte Carlo simulations will not be presented in this paper. Instead, the rest of this paper will focus on additional technical developments that address challenges such as the large phugoid oscillations and enforcement of inequality trajectory constraints.

V. Augmented Predictor-Corrector Guidance

A. Guidance Command Augmentation

In each guidance cycle, let σ_{base} denote the computed bank angle at the current time by the baseline predictor-corrector algorithm from the parameterization in Eq. (19). The baseline aerodynamic lift

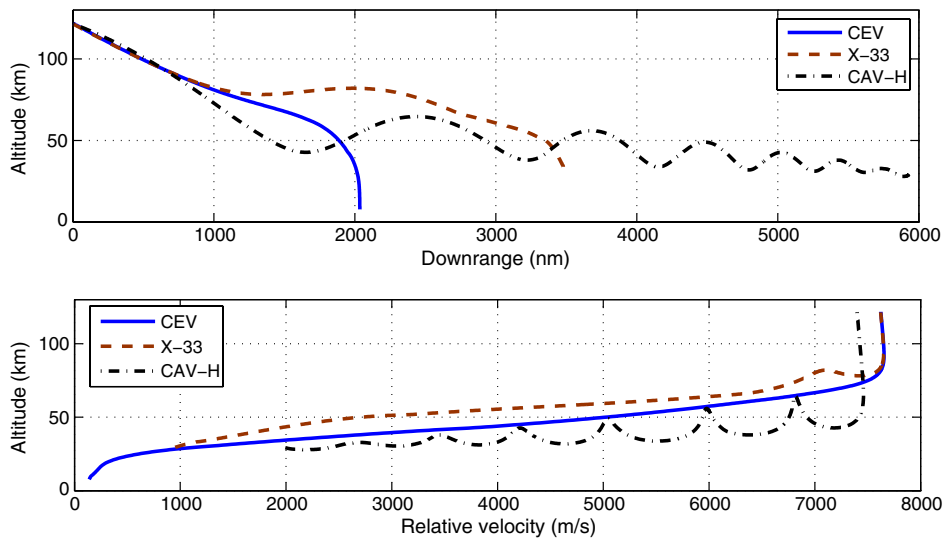


Fig. 3 Orbital entry trajectories of the three vehicles.

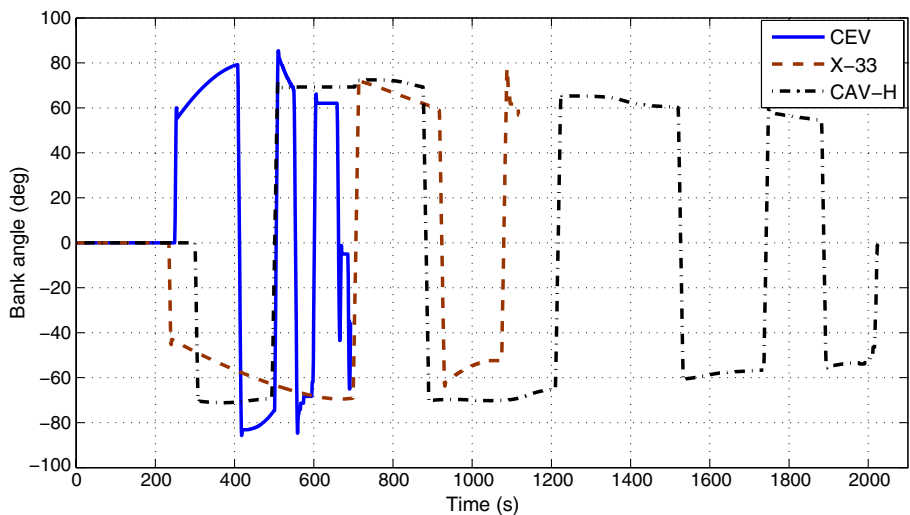


Fig. 4 Bank-angle profiles of the three vehicles.

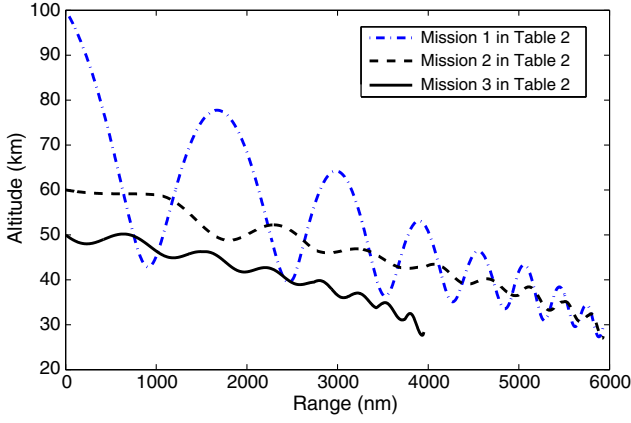


Fig. 5 Suborbital entry scenarios for the CAV-H.

acceleration component in the vertical direction will be $L \cos \sigma_{\text{base}}$, where L is the current total lift acceleration. Another unified feature of this entry guidance method is that any additional need for trajectory shaping is accomplished by augmenting the commanded bank-angle magnitude σ_{cmd} for all types of vehicles and missions, by an altitude-rate compensation in the following form:

$$L \cos \sigma_{\text{cmd}} = L \cos \sigma_{\text{base}} - k(\dot{h} - \dot{h}_{\text{ref}}) \quad (27)$$

where \dot{h} is the current altitude rate, \dot{h}_{ref} is a reference altitude rate that will take different forms for different objectives, and $k > 0$ is a gain. The rationale for Eq. (27) is based on the very essence of entry guidance, that is, modulating the vertical component of the aerodynamic lift force to achieve a desired longitudinal trajectory. With an appropriately designed \dot{h}_{ref} , the compensation term $k(\dot{h} - \dot{h}_{\text{ref}})$ will complement the baseline guidance algorithm to shape the altitude profile for the improved trajectory characteristics or enforcement of inequality trajectory constraints. For different purposes, the specific \dot{h}_{ref} in Eq. (27) will be different. Clearly, if $k = 0$ or \dot{h}_{ref} is selected to be the same as \dot{h} , $\sigma_{\text{cmd}} = \sigma_{\text{base}}$. Thus, the flexibility of returning to the baseline guidance is retained.

The rest of this section is devoted to design an \dot{h}_{ref} to eliminate the large phugoid oscillations observed in the preceding section. The next section will address the enforcement of the inequality trajectory constraints in Eqs. (14–16) by another \dot{h}_{ref} .

B. Equilibrium Glide for Medium to High L/D Ratio Vehicles

The objective in this section is to use the mechanism of Eq. (27) to eliminate the phugoid oscillations in entry trajectories of medium to high L/D ratio vehicles. To find a meaningful \dot{h}_{ref} , consider the equilibrium glide condition, which is obtained by setting $\dot{\gamma} = 0$ and ignoring the Earth-rotation terms in Eq. (5):

$$L \cos \sigma + \left(V^2 - \frac{1}{r} \right) \frac{\cos \gamma}{r} = 0$$

In the previous equation, set $\sigma = \sigma_{\text{QEGC}} = \text{a constant}$ (less than 90 deg) and approximate $r \approx 1$ (recall that r is nondimensional, and $r = 1$ corresponds to the radius of the Earth R_0) and $\gamma \approx 0$. The result may be called the QEGC:

$$L \cos \sigma_{\text{QEGC}} + (V^2 - 1) = 0 \quad (28)$$

Differentiate Eq. (28) once using the expression $L = R_0 S_{\text{ref}} C_L \rho V^2 / 2m$ (where the dimensional atmospheric density ρ is a function of the dimensionless r) and Eqs. (1) and (4), where the Earth-rotation term is omitted. The lift coefficient C_L is treated as a constant. The result gives rise to the required flight-path angle to fly the QEGC in Eq. (28),

$$\sin \gamma_{\text{QEGC}} = \frac{V^2 + L \cos \sigma_{\text{QEGC}}}{(V^2/2)(\beta_r \cos \sigma_{\text{QEGC}})} \left(\frac{1}{C_L/C_D} \right) \quad (29)$$

where

$$\beta_r(r) = \frac{\partial \rho / \partial r}{\rho} \quad (30)$$

For the Earth, the dimensionless parameter β_r is in the range of $-1000 \sim -800$ between the altitude of 25 ~ 80 km, where equilibrium glide can take place. If Eq. (28) is employed again to simplify the numerator of Eq. (29), it reduces to

$$\sin \gamma_{\text{QEGC}} = \frac{1}{(V^2/2)(\beta_r \cos \sigma_{\text{QEGC}})} \left(\frac{1}{C_L/C_D} \right) \quad (31)$$

For $\sigma_{\text{QEGC}} = 0$ and $\sin \gamma_{\text{QEGC}} \approx \gamma_{\text{QEGC}}$, the γ_{QEGC} in Eq. (31) is exactly the first-order solution for the motion in the vertical plane for shallow entry derived in [36]. At high speeds, the values of γ_{QEGC} produced by Eqs. (29) and (31) are very close. They differ only at lower speeds. Figure 6 compares the two histories of γ_{QEGC} computed from Eqs. (29) and (31) along the same entry trajectory for the CAV-H. For subsequent purposes, $\sin \gamma_{\text{QEGC}}$ is used only at high speeds. So either of Eqs. (29) and (31) can be used with equally good effect.

Define the altitude rate required to fly the QEGC by

$$\dot{h}_{\text{QEGC}} = V \sin \gamma_{\text{QEGC}} \quad (32)$$

where V is the current actual velocity. Let $\dot{h}_{\text{ref}} = \dot{h}_{\text{QEGC}}$. Then, Eq. (27) becomes

$$L \cos \sigma_{\text{cmd}} = L \cos \sigma_{\text{base}} - k(\dot{h} - \dot{h}_{\text{QEGC}}) \quad (33)$$

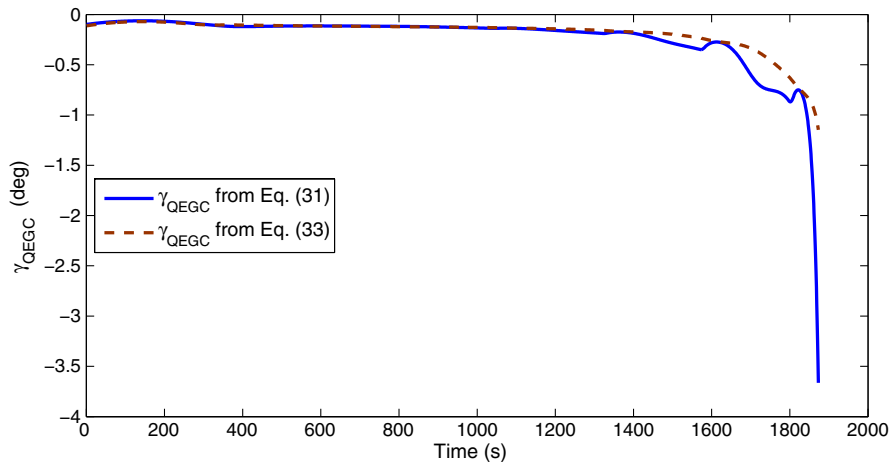


Fig. 6 γ_{QEGC} computed from Eqs. (29) and (31) along the same hypersonic gliding trajectory of the CAV-H.

where \dot{h} is the current altitude rate from the navigation system. The gain $k > 0$ may be scheduled as a linear function of velocity,

$$k = \begin{cases} k_0 + \left(\frac{V_0 - V}{V_0 - V_1}\right)(k_1 - k_0), & V_0 \leq V \leq V_1 \\ 0, & V < V_1 \end{cases} \quad (34)$$

where $k_0 > k_1 \geq 0$, and $V_1 > V_f^*$. A typical value for V_1 is $V_1 = V_f^* + 1000$ m/s for medium to high L/D ratio vehicles. The appropriate value for k_0 can be determined by simulations for a given vehicle, and any $k_1 = 0 \sim 0.5k_0$ will suffice. The value of $k_0 = 20$ (dimensionless) is used for both the CAV-H and X-33 in the simulations in this paper. The performance is not sensitive to the selections of k_0 , k_1 , and V_1 . The gradually diminishing gain designed in Eq. (34) is based on the observation that the most important period in which the altitude-rate compensation in Eq. (33) is needed is the initial phase, in terms of the velocity, of the gliding flight. Once the trajectory has entered a nearly equilibrium glide for some time, it will not start the phugoid oscillations again. This is when the feedback term in Eq. (33) is no longer required and the trajectory control should focus on the ranging requirement, which is the basis of how σ_{base} is generated. Note that the objective of the feedback term in Eq. (33) is not to closely track \dot{h}_{QEGC} but to provide sufficient trajectory damping. This is the reason why the selection of the value for k in Eq. (33) is not sensitive.

The magnitude of the commanded bank angle σ_{cmd} is now computed from Eq. (33). The commanded bank angle will steer the trajectory to fly with an altitude rate close to that of a quasi-equilibrium glide trajectory, which will be free of large phugoid oscillations. Although different choices of σ_{QEGC} in Eq. (29) or (31) can shift the altitude profile of the entry trajectory up and down slightly, the influence is rather minor and practically insignificant. This is because the $\sin \gamma_{\text{QEGC}}$ computed is always small for $\sigma_{\text{QEGC}} < 80^\circ$. For the simulations in this paper, $\sigma_{\text{QEGC}} = 60^\circ$ is used for both the CAV-H and X-33.

Figure 7 compares the altitude profiles of the orbital entry case for the CAV-H with and without the feedback augmentation in the commanded bank angle from Eq. (33). The initial and specified final conditions are the same as those in Sec. IV. The contrast is very sharp: the large phugoid oscillations are eliminated altogether. The high terminal accuracy in range remains the same. It is instructive to look closely at the comparison of the corresponding bank-angle profiles plotted in Fig. 8. Aside from a shift in timing (phase), the only other more visible difference in the bank angle with and without the use of the compensation in Eq. (33) lies in the initial period during which the vehicle just descends into the dense atmosphere and the closed-loop guidance is first called (recall that closed-loop guidance is not called until the aerodynamic acceleration reaches the threshold of 1.52 m/s^2). Without the compensation in Eq. (33), the trajectory pulls up too high after the initial dive and then continues the oscillatory cycles for the rest of the trajectory. With the altitude-rate feedback in the bank angle computed from Eq. (33), the phugoid oscillations are effectively damped out in the entry trajectory of a high L/D ratio vehicle such as the CAV-H, as seen in Fig. 7.

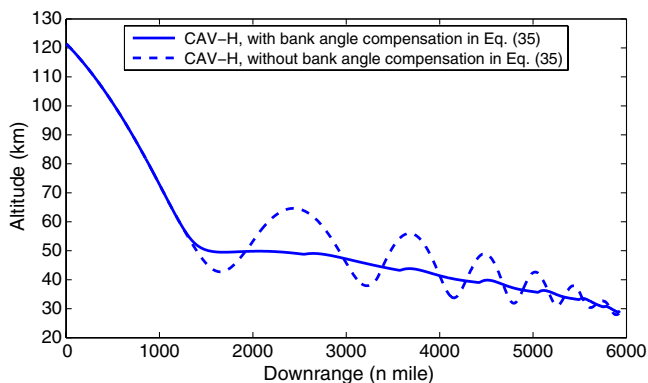


Fig. 7 Altitude histories of the CAV-H in the orbital entry mission.

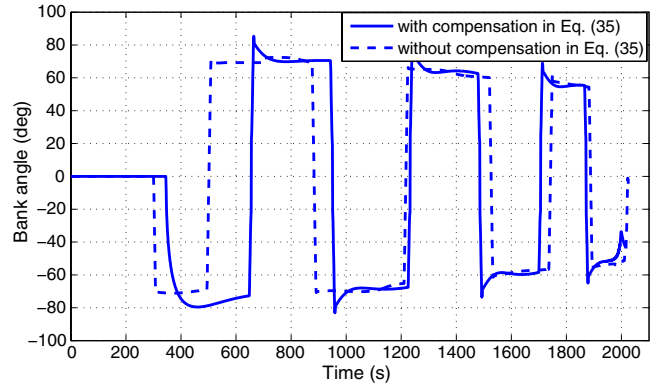


Fig. 8 Bank-angle profiles of the CAV-H in the orbital entry mission.

The feedback compensation in Eq. (33) works for suborbital missions as well. Figure 9 shows the altitude profiles for the same three suborbital missions in Table 2 for the CAV-H (Fig. 5 shows the uncompensated trajectories). Again, the improvements are dramatic. The comparison of the flight-path angle histories for the mission starting at 100 km in altitude and $V_0 = 7010$ m/s are illustrated in Fig. 10, in which γ_{QEGC} from Eq. (31) is also plotted. As a result of Eq. (33), the actual flight-path angle closely follows γ_{QEGC} after the initial dive and before the last part of the trajectory in which the feedback term in Eq. (33) is eased out. The trajectory essentially flies on an equilibrium glide for most of the trajectory with a small negative flight-path angle. The small spikes in the flight-path angle correspond to the bank reversals when the vertical lift component temporarily increases as the bank angle rotates through the attitude of zero bank angle. The consistency of the good performance under the entry guidance command in Eq. (33) for the CAV-H is demonstrated further in more stressful suborbital entry cases in [32].

Figure 11 compares the altitude variations of the X-33 with and without the bank-angle compensation in Eq. (33) in the same mission as in Sec. IV. For this medium L/D ratio vehicle, the major improvement is in the smooth transition from initial descent to the near equilibrium glide phase, in which the altitude loft is eliminated. Such an altitude loft is prone to occur along the entry trajectories of medium L/D ratio vehicles such as the shuttle or X-33 if the bank angle is not carefully planned. One of the adverse consequences of this altitude jump is that the peak heating rate can get unacceptably high after the vehicle drops deeper back into the dense atmosphere from the altitude loft. In [21] and [31], considerable efforts are spent in search of an automated and effective way to suppress this altitude pullup right after the initial descent. The approach presented in Eq. (33) is much simpler and more effective.

In [37], a much more tedious expression for an equilibrium glide flight-path angle γ_{EG} is produced, and the angle of attack is augmented with a feedback term proportional to $(\gamma - \gamma_{\text{EG}})$ for reducing phugoid oscillations in two-dimensional (vertical plane) flight. Aside

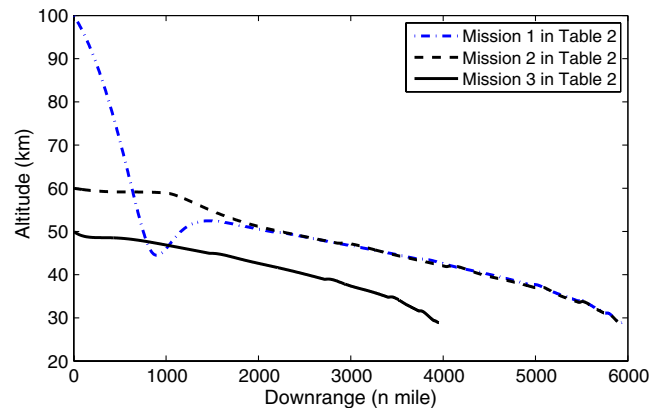


Fig. 9 Altitude histories of the CAV-H in suborbital missions, with compensation in Eq. (33).

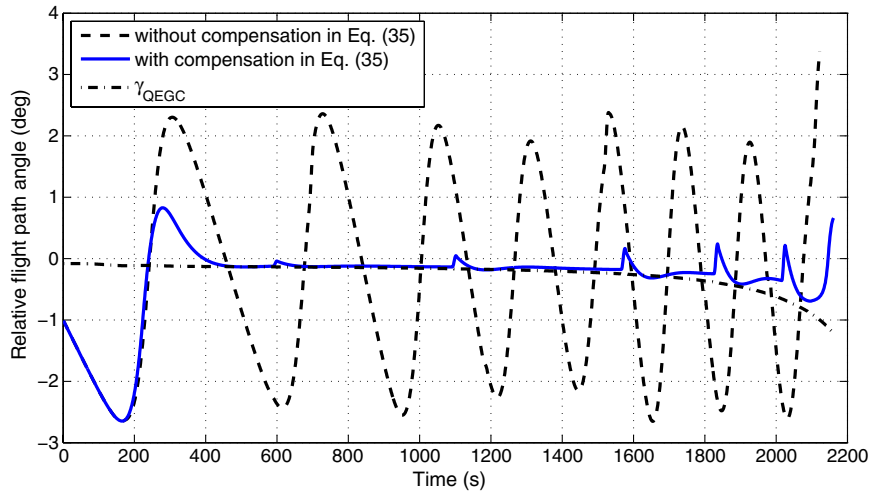


Fig. 10 Flight-path angle histories of the CAV-H in suborbital mission with $h_0 = 100$ km and $V_0 = 7010$ m/s.

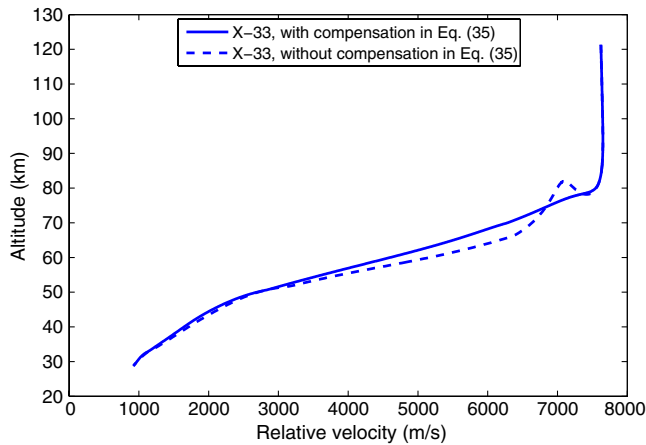


Fig. 11 Altitude histories of the X-33.

from requiring angle-of-attack modulation, this approach will fail if the vehicle flies at an angle of attack corresponding to the maximum lift coefficient, as there will be no room for further increase of the lift when it is called for. Since any practical entry flight will have nonzero bank angle, α modulation (in a limited range) would provide just a fraction of the intended compensation in the vertical direction and hence would be ineffective in general.

The augmented guidance in Eq. (33) is not needed for low L/D ratio vehicles like the CEV (see the already monotonic trajectory of the CEV in Fig. 3). On the other hand, a different h_{ref} in Eq. (27) will prove to be effective for limiting the load factor for capsule vehicles. This topic will be investigated in the next section as a part of a more general approach of enforcing inequality trajectory constraints for entry vehicles.

VI. Heating and Load Management

In this section, the attention is on managing the heating rate and load factor along the trajectory so they will not have excessively large peak values. The guiding principles for devising the method are 1) it must be technically rigorous and effective, 2) it must not increase the computational requirements significantly, and 3) it must not adversely affect the precision and the robustness of the guidance algorithm. The technical approach is based on the augmented predictor-corrector guidance in Eq. (27) with appropriate choices of h_{ref} . In the following, an added benefit is first noted on reducing the peak heating rate and g -load for lifting-body vehicles by flying an equilibrium glide path under the augmented predictor-corrector guidance (33). Then, the major development is presented on a novel predictive method for reliable enforcement of inequality constraints

on the heating rate, load factor, and dynamic pressure, applicable to any type of entry vehicle, whenever it is physically feasible to do so.

A. Peak Heating and Load Reduction by Equilibrium Glide

One of the driving motivations to use the guidance compensation in Eq. (33) is to shape the trajectory to avoid excessive heating and load stresses for medium to high L/D ratio vehicles. It will be illustrated that, by steering the trajectory quickly onto equilibrium glide, the augmented bank-angle command from Eq. (33) can indeed significantly reduce the peak values for the heating rate and load factor, as well as dynamic pressure in some cases.

Figures 12 and 13 show the comparison of heating rate, load factor, and dynamic pressure with and without the compensation in Eq. (33) for the CAV-H and X-33. For the CAV-H with compensation, the reduction in the peak heating rate is from 7022.7 to 4704.5 kW/m² (618 to 414 Btu/ft² · s, a 33% reduction), peak load factor from 3.5 to 1.56g (a 55% reduction), and peak dynamic pressure from 158.004 to 68.468 kN/m² (3300 to 1430 psf, a 57% reduction). For the X-33, the peak heating rate reduces from 1097.7 to 772.7 kW/m² (96.6 to 68 Btu/ft² · s), and the peak load factor reduces from 2.8 to 2.3g (the peak dynamic pressure remains about the same). For both the CAV-H and X-33, the relatively flat heating-rate profiles with compensation suggest that the peak heating rates are already close to the lowest possible values in the respective case. In fact, for the CAV-H, the solid curve in the top subplot of Fig. 12 indicates that the peak heating rate for this particular set of entry conditions cannot be lowered further since the peak occurs right at the end of the initial descent, and, with zero bank angle in initial descent, the vehicle is already flying with full lift vector up.

Under the guidance command from Eq. (33), these relatively flat heating profiles are found to be a consistent occurrence for medium and high L/D ratio vehicles. By steering the trajectory onto an equilibrium glide path at high speeds, the heating-rate profile would stay close to the average values instead of going through valleys and peaks. This is evident from Figs. 12 and 13: while peak heating rates with compensation are significantly lower than the ones without, the total heating loads (the integration of the heating rate over time) stay approximately the same, which reflects the fact that a given amount of energy dissipation is required for each entry mission, independent of the actual trajectory flown.

B. Predictive Load Relief

Although the equilibrium glide compensation in Eq. (33) is shown to be able to significantly reduce the peak heating, load, and sometimes the dynamic pressure for medium to high L/D ratio vehicles, there may be cases in which further reduction is desired or specific limits must be ensured in all feasible cases. Then, of course, there are low L/D ratio vehicles for which the compensation in Eq. (33) is not reliably effective in reducing peak heating and

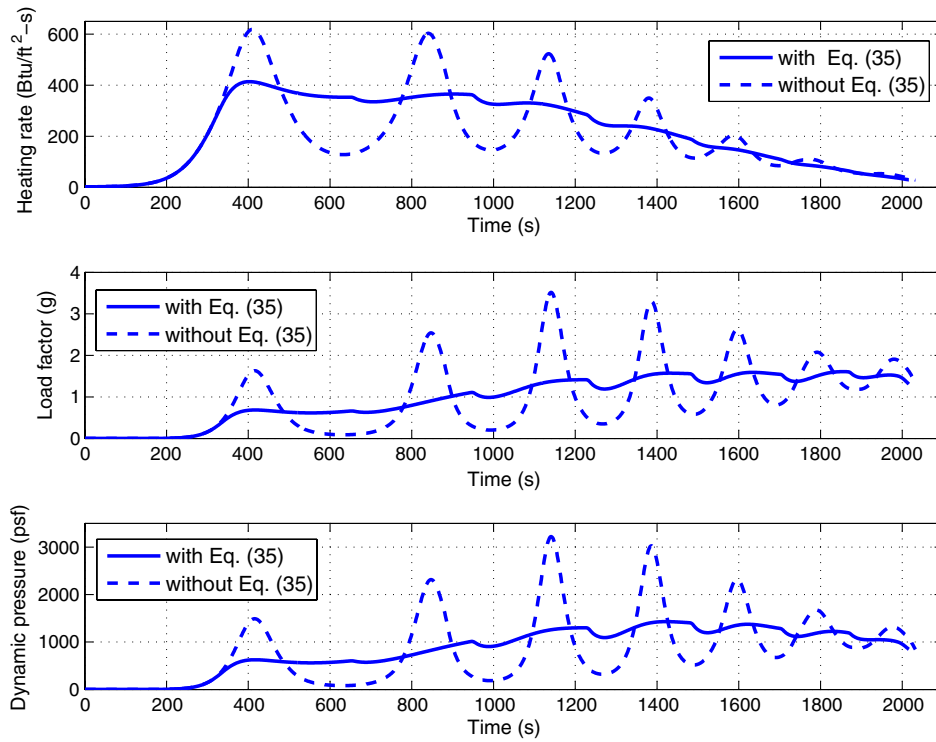


Fig. 12 Heating rate, load factor, and dynamic pressure for CAV-H orbital entry, with and without bank-angle compensation in Eq. (33).

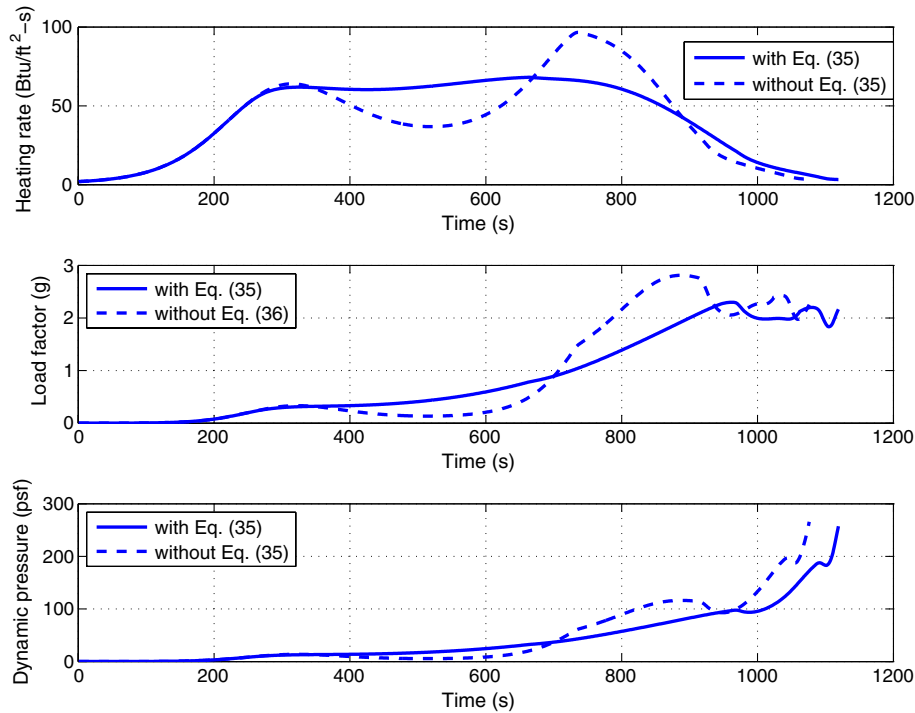


Fig. 13 Heating rate, load factor, and dynamic pressure for X-33 with and without bank-angle compensation in Eq. (33).

dynamic loads. In short, a more quantifiable, precise, and universally applicable approach is still needed.

It is known that, for constant aerodynamic coefficients, the peak heating rate occurs before the peak load factor during entry flight [38]. For capsules with subcircular entry speeds, the peak heating rate is largely a function of the entry condition and is difficult to be lowered significantly by the trajectory control (bank angle) [30]. This is because the peak heating rate for a capsule vehicle usually occurs at the pullup immediately following the initial descent. There is little

aerodynamic trajectory control can do before the peak heating rate to lower it. The peak load factor, however, can still be influenced significantly by the trajectory control. The load limiter approach in Apollo guidance [1], which commands the lift vector fully up when the load factor exceeds the limit, is not reliably effective. Moreover, such logic tends to severely degrade the guidance performance (precision) when the peak load is more than just slightly above the limit. To the best of the author's knowledge, there exists no other more reliably effective guidance approach for the ensured

enforcement of a constraint on the peak load factor for capsule vehicles. For vehicles with medium to higher lifting capabilities, both the peak heating rate and load factor can be influenced by the trajectory, provided that the peak heating rate does not take place at the first pullup after the initial descent.

In this and the next sections, a method is developed that combines elements from a control synthesis based on the separation of time scales in dynamic systems [39], nonlinear predictive control [40], and the augmented predictor-corrector guidance of the form in Eq. (27). A predictive load-relief approach is first developed in this section for the accurate satisfaction of the load factor constraint for capsule vehicles while ensuring guidance precision. Then, the method is readily expanded to cover the heating-rate, load-factor, and dynamic-pressure constraints in the next section for lifting-body vehicles.

The first step is to regard the flight-path angle dynamics in Eq. (5) as fast dynamics and the altitude dynamics in Eq. (1) as slow dynamics. This is certainly justifiable physically. By following the control synthesis methodology developed in [39] for such two-time-scale systems, treat $\sin \gamma$ as the pseudocontrol in the slow altitude dynamics,

$$\dot{r} = V u_\gamma \quad (35)$$

where $u_\gamma = \sin \gamma$. The idea is to first find the u_γ required to produce the altitude rate such that an altitude-dependent inequality trajectory constraint will be satisfied. Then, appropriate trajectory control, the bank angle, is generated to realize this required u_γ . First, consider the load factor constraint in Eq. (15) with $a = \sqrt{L^2 + D^2}$, which is a function of r and V , for a given α profile. Differentiating a with respect to time gives

$$\dot{a} = -\frac{2aD}{V} + aV\beta_r u_\gamma := A_a + B_a u_\gamma \quad (36)$$

where C_L and C_D have been treated as constant, the approximation of $\dot{V} = -D$ based on Eq. (4) is justifiably used, and β_r is the same as defined in Eq. (30). Note that both $A_a < 0$ and $B_a < 0$. Let $\delta > 0$ be a specified prediction horizon parameter. A first-order prediction for $a(t + \delta)$ is then

$$a(t + \delta) = a(t) + \dot{a}\delta = a + A_a\delta + \delta B_a u_\gamma \quad (37)$$

The objective is to maintain the inequality constraint $a(t + \delta) \leq a_{\max}$. Equation (37) leads to the requirement on the pseudocontrol:

$$u_\gamma \geq \frac{a_{\max} - a - A_a\delta}{B_a\delta} = \frac{a_{\max} - a(1 - 2D\delta/V)}{aV\beta_r\delta} := U_a \quad (38)$$

At any point along the trajectory, define a reference flight-path angle by

$$\sin \gamma_{\text{ref}} = \max\{\sin \gamma, U_a\} \quad (39)$$

where γ is the current actual flight-path angle. Note that $\sin \gamma_{\text{ref}}$ is continuous despite the “max” operation in Eq. (39) because both $\sin \gamma$ and U_a are continuous. For sufficiently small δ , $\sin \gamma_{\text{ref}} = \sin \gamma$ from Eq. (39) when the current load factor a is sufficiently smaller than a_{\max} . This is because U_a has a more negative value in such a case (recall that $\beta_r < 0$) than $\sin \gamma$, which has a small negative value that is very close to zero. Only when the load factor a gets close to a_{\max} is it possible that $\sin \gamma_{\text{ref}} = U_a$. Define a reference altitude rate by

$$\dot{h}_{\text{ref}} = V \sin \gamma_{\text{ref}} \quad (40)$$

where V is the current velocity. Note that \dot{h}_{ref} is equal to the current actual altitude rate \dot{h} when $\sin \gamma_{\text{ref}} = \sin \gamma$. The reference altitude rate in the Eq. (40) represents the desired altitude rate if the altitude in

the near future is to be such that the constraint $a(t + \delta) \leq a_{\max}$ is satisfied. To achieve the altitude rate in Eq. (40), a bank-angle control law in Eq. (27) is used,

$$L \cos \sigma_{\text{cmd}} = L \cos \sigma_{\text{base}} - k_0(\dot{h} - \dot{h}_{\text{ref}}) \quad (41)$$

where $k_0 > 0$ is a constant gain. A discussion on how to implement and use Eq. (41) is in order:

1) A major difference between the use of Eqs. (33) and (41) is where to apply them. Compensation in Eq. (33) can be safely applied outside the baseline predictor-corrector algorithm; that is, σ_{base} is from the converged predictor-corrector guidance solution. This is because the term $k(h - h_{\text{QEGC}})$ in Eq. (33) has tangible but still relatively small effects on the bank angle just in an initial period (cf. Fig. 8), and \dot{h} need not track \dot{h}_{QEGC} closely. On the other hand, \dot{h} needs to track \dot{h}_{ref} closely for the current purpose. Consequently, the excursions in the bank angle caused by the term $k_0(\dot{h} - \dot{h}_{\text{ref}})$ can be substantial. Hence, Eq. (41) should be used in the solution process of the predictor-corrector algorithm when the integrations of the trajectory are performed. Thus, in implementing Eq. (41), σ_{base} is the value from the bank-angle parameterization in Eq. (19). Then, σ_{cmd} is computed from Eq. (41) along the propagated trajectory and used in the numerical integrations of the algorithm. This is a critically important distinction and a key for the success of this approach.

2) Although the previous derivation based on the predictive control approach uses a finite prediction horizon δ in the interval $[t, t + \delta]$, it should be stressed that the constraint is enforced throughout the rest of the predicted trajectory in the predictor-corrector solution process (not just in a fixed interval of length δ), as t is sliding forward to the end in the trajectory integrations and Eq. (41) is applied at each point along the predicted trajectory. This is different from the receding-horizon control problem in which the problem is indeed just solved over a finite horizon at each instant.

3) Once the predictor-corrector guidance algorithm in the previous step converges, Eq. (41) is used one more time to generate the guidance command output σ_{cmd} for the current cycle. In this pass, σ_{base} will be the bank angle at the current time from the converged predictor-corrector solution, and other quantities are all computed based on navigation data instead of onboard models. When $\dot{h}_{\text{ref}} = VU_a$ in Eq. (41) and the expression for U_a in Eq. (38) is used, Eq. (41) can be written explicitly as

$$L \cos \sigma_{\text{cmd}} = L \cos \sigma_{\text{base}} - k_1(a_{\max} - a) - k_0\left(\dot{h} - \frac{2D}{aV\beta_r}\right), \quad (42)$$

$$k_1 = \frac{k_0}{a\delta\beta_r}$$

The values of L , D , a , V , and \dot{h} used in the Eq. (42) in this last pass are all from the current navigation data. The purpose of this step is to use the sensed data for computing the quantities in Eq. (42) (especially the g -load a) instead of relying on onboard models for a final correction on the guidance command. This step would be practically important to reduce the effects of the inevitable modeling uncertainty in the atmospheric density and aerodynamic coefficients.

4) If the actual load factor a does not get close to a_{\max} , Eq. (39) will produce $\sin \gamma_{\text{ref}} = \sin \gamma$ as pointed out before. Therefore, $\dot{h}_{\text{ref}} = \dot{h}$ by definition [cf. Eq. (40)]. The guidance command generated from Eq. (41) will automatically reduce to that of the baseline algorithm, as if the load factor constraint were not imposed. In other words, the guidance command from Eq. (41) will not unnecessarily seek to ride on the constraint boundary.

5) Instead of gradually reducing the gain k as in Eq. (34), the controller gain k_0 in Eq. (41) should be kept constant for the period during which the inequality constraint may be expected to be active because the purpose now is to track \dot{h}_{ref} reasonably closely.

6) If the pseudocontrol is perfectly realized, i.e., \dot{h}_{ref} is perfectly tracked, it is shown in [40] that strict enforcement of the type of constraints, such as $a \leq a_{\max}$ here, and $\dot{Q} \leq \dot{Q}_{\max}$ and $\bar{q} \leq \bar{q}_{\max}$ in the next section, is guaranteed by this predictive control approach for any $\delta > 0$ (assume, of course, that they are all feasible). Since the tracking

of \dot{h}_{ref} by the simple proportional control mechanism in Eq. (41) cannot be perfect, there may be some violations of $a \leq a_{\text{max}}$ in some cases. But they can be kept small by selecting appropriate values for δ and k_0 and adding a small margin in a_{max} of 0.1g or so. A smaller δ produces a tighter enforcement of the constraint but tends to demand faster bank-angle modulations and vice versa. For a given vehicle, the selections of δ and k_0 are again relatively easy by numerical trials that strike a balance between reasonable tightness of the constraint enforcement and acceptable control (bank-angle) response.

The previously described predictive load-relief method is applied to the CEV in the mission first shown in Fig. 3. A value of $\delta = 0.02$ (nondimensional, 16 s in real time) and $k_0 = 100$ (nondimensional) are used. Figure 14 compares three different profiles of the load factor, one unconstrained ($a_{\text{max}} = +\infty$), another constrained with $a_{\text{max}} = 4.0g$, and the last with $a_{\text{max}} = 3.0g$. The unconstrained trajectory has a peak load factor of 5.4g. The previously developed load-relief method is effective in enforcing the load factor constraint in both constrained cases. The guidance precision in terms of the final miss distance to the landing site for all three cases is within 1.5 km or less (recall that these are nominal cases without navigation errors and modeling uncertainties). For this mission, the lowest peak load factor enforcible with the method developed here is about 2.8g, which should be about the lowest feasible g load this mission can accommodate, judging from Fig. 14.

Figure 15 illustrates the bank-angle profiles in the three cases. As expected, when the load-factor constraint is imposed, the bank-angle profile changes considerably. A visible pattern of change is in the initial magnitude of the bank angle as soon as the closed-loop guidance is called around 250 s. This magnitude becomes larger as $a \leq a_{\text{max}}$ is enforced and a_{max} is smaller. This increase of the initial bank-angle magnitude would force the trajectory to dive deeper into the dense atmosphere initially, thus depleting more energy while the dynamic pressure (and the load factor) has not yet reached its high value. This allows the trajectory to be more lofted in the middle portion of the flight so as to reduce the peak value of the load factor. The altitude-vs-velocity profiles in Fig. 16 confirm that this is what happens. Such an anticipatory behavior in the trajectory control is

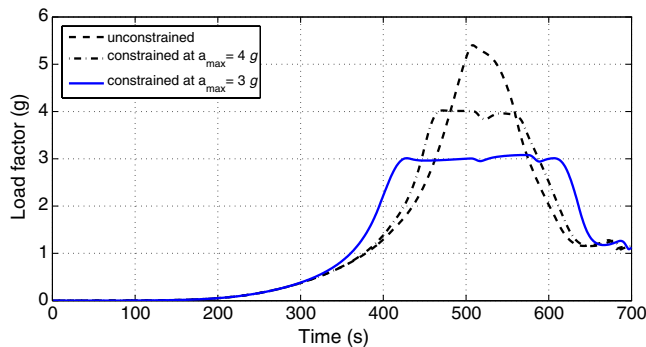


Fig. 14 Load-factor profiles for the CEV with and without predictive load relief.

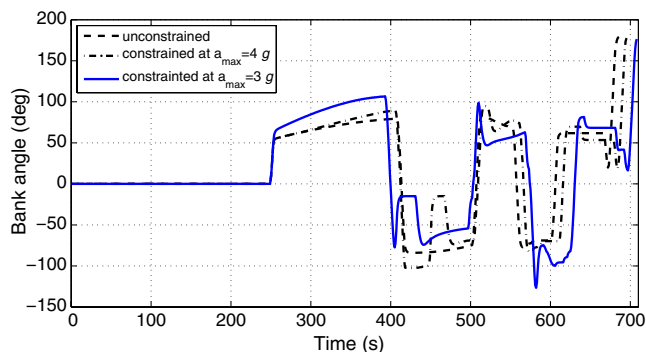


Fig. 15 Bank-angle profiles for the CEV with and without predictive load relief.

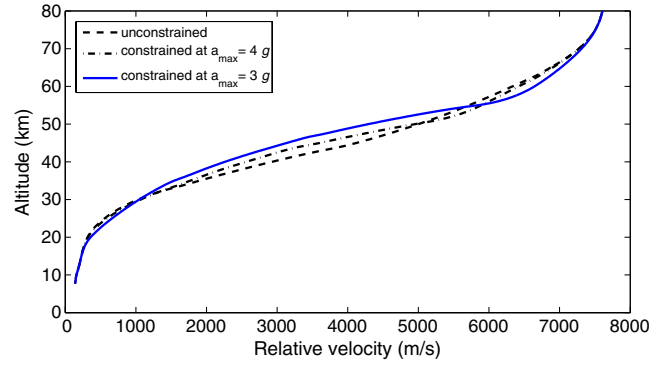


Fig. 16 Altitude-vs-velocity profiles for the CEV with and without predictive load relief (the portion at higher altitudes is truncated).

exactly what a predictive approach is expected to have, as opposed to a reactive technique like the Apollo load limiter, and it enables this load-relief measure to significantly reduce the g load as needed and still maintain high guidance precision.

In [30], it is observed that during the initial descent from the entry interface to 80 km or so in altitude, if a nonzero bank angle is used, the peak load factor tends to be reduced somewhat. The underlying reason is similar to what was noted previously; that is, a nonzero initial bank angle would make the trajectory dive deeper into the dense atmosphere initially, causing a higher trajectory later. But that simplistic and open-loop approach cannot guarantee a specified amount of reduction in the peak load, and the effectiveness is rather limited. The more sophisticated (yet still simple) predictive load-relief method developed in this section will produce a predictable peak load factor as specified, provided that the required load factor constraint still permits a feasible trajectory.

The predictive load-relief approach developed here enjoys a property that is important in practice. When the constraint $a \leq a_{\text{max}}$ is infeasible, that is, it cannot be met all the time with the given initial condition in a mission, the proposed algorithm will attempt to fly the g-load limit whenever possible while still trying its best to meet the downrange requirement. Such graceful degradation, as opposed to a catastrophic failure of abruptly breaking down and ceasing to function, instills confidence in practical applications. Figure 17 illustrates this point by three increasingly infeasible cases for the CEV when a_{max} is reduced (the initial condition remains the same). The performance of the guidance algorithm, in terms of the final miss distance, degrades only gradually as the infeasibility grows larger.

C. Predictive Enforcement of Inequality Trajectory Constraints

In the previous development, if a and a_{max} are replaced by \dot{Q} and \dot{Q}_{max} , or \bar{q} and \bar{q}_{max} , the same process can be applied to the heating rate and dynamic pressure to enforce the constraints in Eqs. (14) and (16) just as well. By following the same procedure that yields Eq. (38), two similar quantities can be obtained:

$$U_{\dot{Q}} = \frac{\dot{Q}_{\text{max}} - \dot{Q}(1 - 3.15D\delta/V)}{(1/2)\dot{Q}V\beta_r\delta} \quad (43)$$

$$U_{\bar{q}} = \frac{\bar{q}_{\text{max}} - \bar{q}(1 - 2D\delta/V)}{\bar{q}V\beta_r\delta} \quad (44)$$

Define

$$\sin \gamma_{\text{ref}} = \max\{\sin \gamma, U_a, U_{\dot{Q}}, U_{\bar{q}}\} \quad (45)$$

Then, the guidance command from Eq. (41) will have the ability to enforce the three constraints in Eqs. (14–16) for medium to high L/D ratio vehicles. Note that U_a and $U_{\bar{q}}$ will be the same if the aerodynamic coefficients are constant and the ratio $a_{\text{max}}/\bar{q}_{\text{max}} = \sqrt{C_L^2 + C_D^2}$. This is why $U_{\bar{q}}$ is not always used.

In using Eq. (41) with $\sin \gamma_{\text{ref}}$ defined in Eq. (45), all the points in the discussion in the preceding section still apply. Furthermore, in

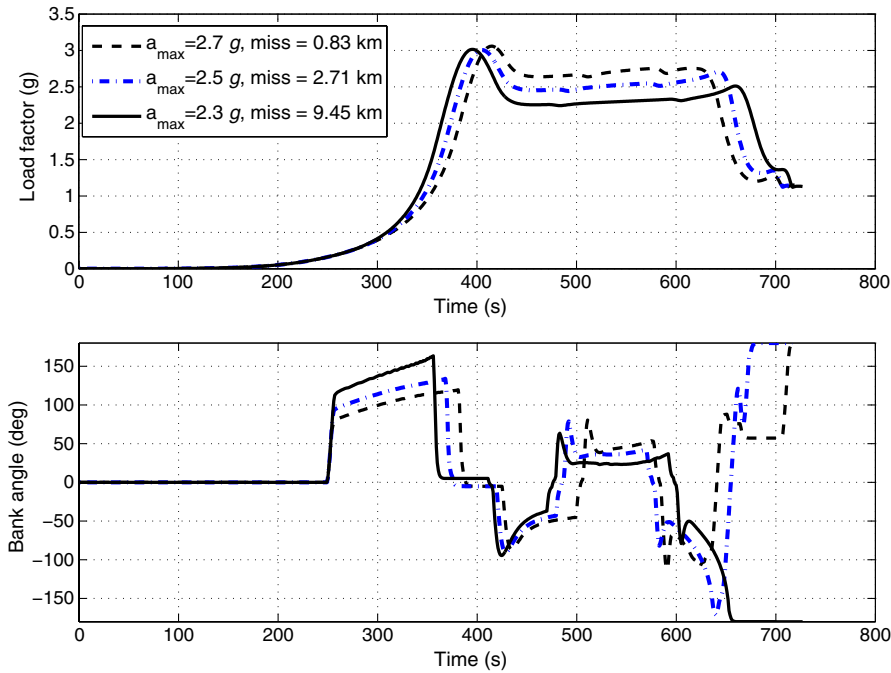


Fig. 17 Load-factor and bank-angle profiles for CEV in infeasible cases in which the constraint $a \leq a_{\max}$ cannot be met all the time.

point 3 of the discussion before applying Eq. (41) one more time to generate the guidance command, it is highly recommended that Eq. (33) be used once for medium to high L/D ratio vehicles as an intermediate step. In doing so, the σ_{base} to be used in Eq. (41) is the output (σ_{cmd}) from Eq. (33). This action has the benefit of still providing the necessary trajectory damping (especially for high L/D ratio vehicles like the CAV-H) when the augmentation in Eq. (41) is not active (i.e., the constraint is not active and $\dot{h}_{\text{ref}} = \dot{h}$). Another benefit of successively using Eq. (33) and then Eq. (41) is that the final guidance command for the bank angle from Eq. (41) tends to be more well behaved and benign, as the compensation of Eq. (33) already shaped the trajectory to have relatively low and flat heating-rate and load-factor profiles, as seen in Sec. VI.A.

A value of $\delta = 0.02$ (nondimensional, 16 s in real time) is again used in the definitions of U_d and $U_{\dot{Q}}$ for the X-33, and a $k_0 = 40$ (nondimensional) is used in Eq. (41). Figure 18 shows the heating-rate and load-factor profiles of the X-33 under the baseline guidance [unconstrained, without augmentation in Eq. (33)], subject to only the heating rate constrained with $\dot{Q}_{\max} = 726,784 \text{ W/m}^2$ (64 Btu/ft \cdot s 2) and subject to both the heating rate and load factor constrained with $\dot{Q}_{\max} = 726,784 \text{ W/m}^2$ and $a_{\max} = 2.0g$. It

should be pointed out that this \dot{Q}_{\max} is the lowest peak heating rate the X-33 can ever achieve in this particular mission. For the same mission and the X-33 vehicle, the nominal limit of the heating rate specified in [25] is 794,920 W/m 2 (70 Btu/ft \cdot s 2). The previously developed predictive approach works well, as expected. With just the heating-rate constraint, the peak heating rate is kept right at the limit, while the peak load factor is decreased from 2.8g in the unconstrained case to 2.4g, but still greater than 2.0g. When both heating-rate and load factor constraints are imposed, the proposed predictive approach is able to accurately enforce both constraints. The corresponding bank-angle profiles are plotted in Fig. 19. The constrained bank-angle profiles have relatively large differences as compared to the unconstrained one, indicating the substantial impact the enforcement of the inequality constraint(s) has on the trajectory control. The altitude-vs-velocity profiles of the trajectories are given in Fig. 20. It is evident that a predominant portion of the trajectory with both constraints lies on the boundaries of the constraints.

For the CAV-H, the same values of $\delta = 0.02$ and $k_0 = 40$ (nondimensional) are used. Figure 21 shows the heating-rate and load-factor profiles for an orbital entry mission that is slightly different from the one in Fig. 12 in the initial flight-path angle

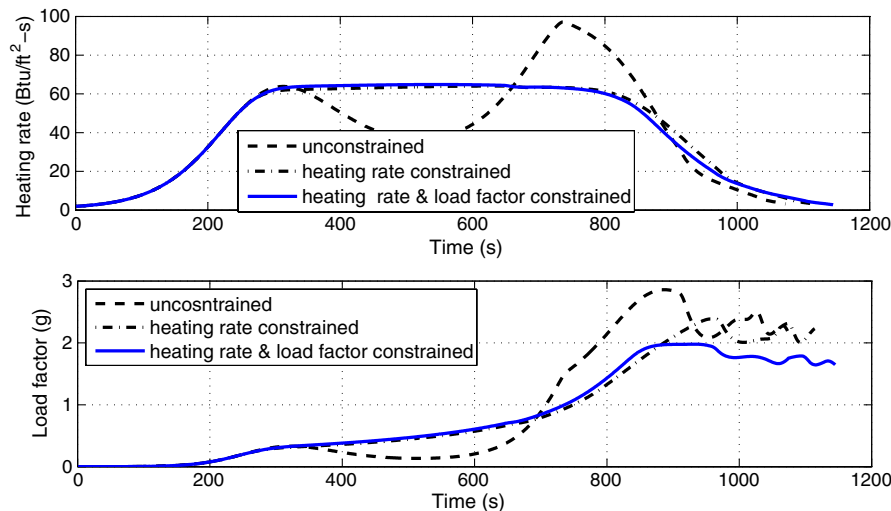


Fig. 18 Heating-rate and load-factor profiles for the X-33 with and without predictive heating and load constraint enforcement.

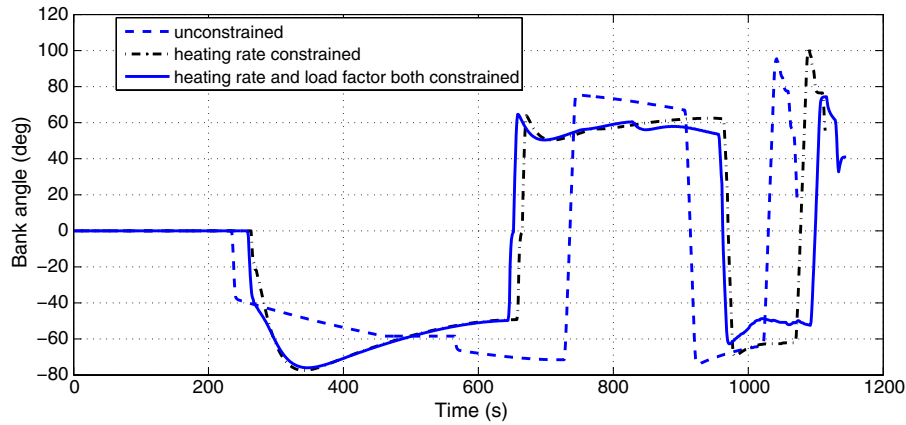


Fig. 19 Bank-angle profiles for the X-33 with and without predictive heating and load constraint enforcement.

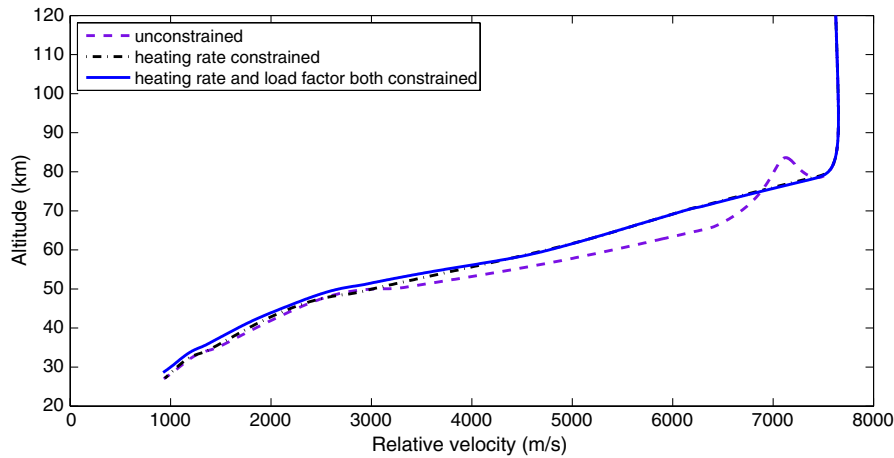


Fig. 20 Altitude-vs-velocity profiles for the X-33 with and without predictive heating and load constraint enforcement.

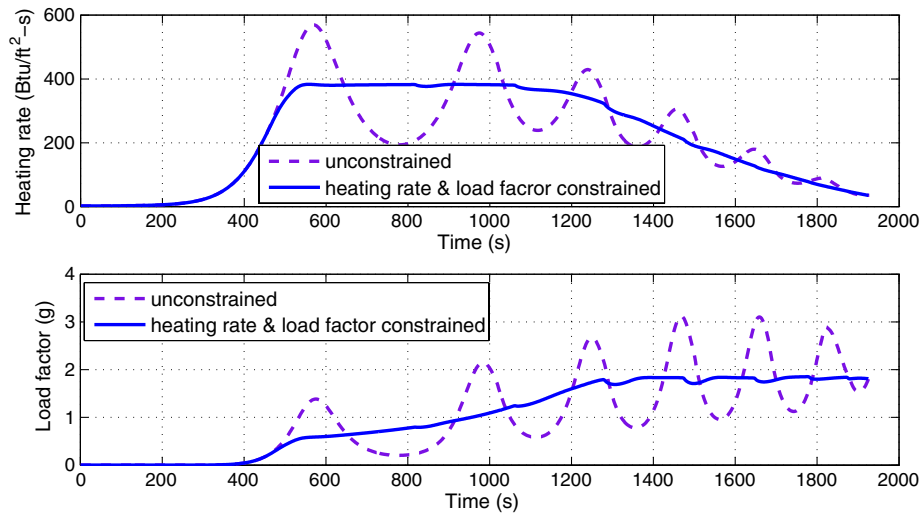


Fig. 21 Heating-rate and load-factor profiles for the CAV-H with and without predictive heating and load constraint enforcement.

(shallower). Under the baseline guidance algorithm (without inequality constraints), the highly oscillatory trajectory is characteristic of the CAV-H, as seen before. In the presence of the heating-rate constraint with a $\dot{Q}_{\max} = 4,315,280 \text{ W/m}^2$ ($380 \text{ Btu/ft}^2 \cdot \text{s}$) and load-factor constraint with $a_{\max} = 1.8g$, the predictive approach is employed to enforce the corresponding heating-rate and load-factor constraints in Eqs. (14) and (15). The effectiveness of the predictive approach for this high L/D ratio vehicle is again clear, as evident

from Fig. 21. The corresponding bank-angle profiles are plotted in Fig. 22. For the dramatic difference in Fig. 21, the bank-angle profiles differ relatively mildly. This has been observed time and again for this high-lifting vehicle, which is also typical for this class of vehicles (their high-lifting capability means that a small difference in the bank-angle profile can cause large changes in the trajectory).

In [31], a QEGC-based velocity-dependent upper bound on the bank-angle magnitude is used to indirectly limit the heating rate, load

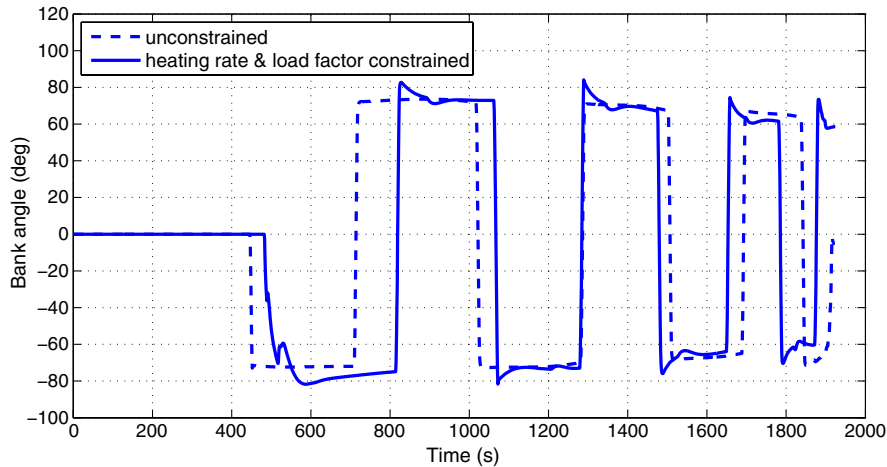


Fig. 22 Bank-angle profiles for the CAV-H with and without predictive heating and load constraint enforcement.

factor, and dynamic pressure. The assumption of equilibrium glide may or may not be sufficiently accurate to render that approach effective in a given case or for a given vehicle. The predictive method developed in this section does not rely on any assumptions such as the QEGC but on active trajectory control/shaping. Therefore, this approach is reliably effective in all cases and for different vehicles with low and high L/D ratios.

Finally, it is worth noting that the predictive control approach in this paper can be applied to enforce any inequality constraint of the form $\eta(r, V) \leq 0$, provided $\partial\eta/\partial r \neq 0$. Furthermore, the enforcement of $\eta(r, V) \leq 0$ may be performed just in certain portions of the trajectory (say, the second half). This general applicability should prove valuable in applications in which additional or different constraints from those in Eqs. (14–16) (for instance, an altitude inequality constraint in a given range of velocity) are desired to be met.

VII. Conclusions

A unified predictor-corrector entry guidance method is developed that is applicable to a wide range of vehicles with low to high L/D ratios and in-orbital as well as suborbital missions. The method uses a simple and robust numerical predictor-corrector algorithm as the baseline algorithm. This baseline algorithm ensures reliable and accurate satisfaction of the fundamental requirement of covering the specified downrange with the specified energy depletion. Additional (and frequently more complex) needs for further trajectory shaping are met by augmenting the baseline algorithm with an altitude-rate-dependent feedback compensation. This augmentation can be designed differently to address different needs while still maintaining the guidance precision afforded by the baseline algorithm. The elimination of large phugoid oscillations for a high L/D ratio vehicle and smooth transition between initial descent and near-equilibrium glide for a medium L/D ratio vehicle are two frequent and important requirements that are effectively accomplished by this augmented guidance method. The long-standing challenge of enforcing common inequality trajectory constraints in predictor-corrector entry guidance has been successfully overcome with the augmentation by a novel predictive altitude-rate compensation technique. As a result, the developed entry guidance method offers reliable enforcement of the load-factor constraint for capsule vehicles and heating-rate and load-factor constraints for medium and high L/D ratio vehicles. The required computational time and resources are comparable to the requirements of a typical numerical predictor-corrector entry guidance algorithm.

Acknowledgment

The author would like to express his sincere thanks to the reviewers and the associate editor of this paper for their many constructive comments and suggestions of both technical and editorial nature.

They have really helped improve the preciseness and readability of the paper.

References

- [1] Moseley, P. E., "The Apollo Entry Guidance: A Review of the Mathematical Development and Its Operational Characteristics," TRW Note No. 69-FMT-791, Houston, TX, Dec. 1969.
- [2] Graves, C. A., and Harpold, J. C., "Apollo Experience Report: Mission Planning for Apollo Entry," NASA TN-D-6725, March 1972.
- [3] Putnam, Z. R., Bairstow, S.H., Braun, R. D., and Barton, G. H., "Improving Lunar Return Entry Range Capability Using Enhanced Skip Trajectory Guidance," *Journal of Spacecraft and Rockets*, Vol. 45, No. 2, 2008, pp 309–315. doi:10.2514/1.27616
- [4] Brunner, C., and Lu, P., "Skip Entry Trajectory Planning and Guidance," *Journal of Guidance, Control, and Dynamics*, Vol. 31, No. 5, 2008, pp. 1210–1219. doi:10.2514/1.35055
- [5] Brunner, C., and Lu, P., "Comparison of Fully Numerical Predictor-Corrector and Apollo Skip Entry Guidance Algorithms," *Journal of Astronautical Sciences* (to be published).
- [6] Tigges, M. A., Crull, T., and Rea, J. R., "Numerical Skip-Entry Guidance," American Astronautical Soc. Paper 07-076, AAS Publication Office, San Diego, CA, Feb. 2007.
- [7] Bairstow, S. H., "Reentry Guidance with Extended Range Capability for Low L/D Spacecraft," S.M. Thesis, Dept. of Aeronautics and Astronautics, Massachusetts Inst. of Technology, Cambridge, MA, Feb. 2006.
- [8] Harpold, J. C., and Graves, C. A., "Shuttle Entry Guidance," *Journal of Astronautical Sciences*, Vol. 37, No. 3, 1979, pp. 239–268.
- [9] Harpold, J. C., and Gavert, D. E., "Space Shuttle Entry Guidance Performance Results," *Journal of Guidance, Control, and Dynamics*, Vol. 6, No. 6, 1983, pp. 442–447. doi:10.2514/3.8523
- [10] Roenneke, A. J., and Markl, A., "Reentry Control of a Drag vs. Energy Profile," *Journal of Guidance, Control, and Dynamics*, Vol. 17, No. 5, 1994, pp. 916–920. doi:10.2514/3.21290
- [11] Roenneke, A. J., "Adaptive On-Board Guidance for Entry Vehicle," AIAA Paper 2001-37343, Aug. 2001.
- [12] Mease, K. D., Chen, D. T., Teufel, P., and Schoenenberger, H., "Reduced-Order Entry Trajectory Planning for Acceleration Guidance," *Journal of Guidance, Control, and Dynamics*, Vol. 25, No. 2, 2002, pp. 257–266. doi:10.2514/2.4906
- [13] Grimm, W., van der Meuller, J. G., and Roenneke, A. J., "Optimal Update Scheme for Drag Reference Profiles in an Entry Guidance," *Journal of Guidance, Control, and Dynamics*, Vol. 26, No. 5, 2003, pp. 695–701. doi:10.2514/2.5123
- [14] Mease, K. D., and Kremer, J. -P., "Shuttle Guidance Revisited Using Nonlinear Geometric Methods," *Journal of Guidance, Control, and Dynamics*, Vol. 17, No. 6, 1994, pp. 1350–1356. doi:10.2514/3.21355

- [15] Bharadwaj, S., Rao, A. V., and Mease, K. D., "Entry Guidance Trajectory Tracking Law via Feedback Linearization," *Journal of Guidance, Control, and Dynamics*, Vol. 21, No. 5, 1998, pp. 726–732. doi:10.2514/2.4318
- [16] Lu, P., "Regulation About Time-Varying Trajectories: Precision Entry Guidance Illustrated," *Journal of Guidance, Control, and Dynamics*, Vol. 22, No. 6, 1999, pp. 784–790. doi:10.2514/2.4479
- [17] Dukeman, G. A., "Profile-Following Entry Guidance Using Linear Quadratic Regulator Theory," AIAA Paper 2002-4457, Aug. 2002.
- [18] Lu, P., "Entry Guidance and Trajectory Control for Reusable Launch Vehicle," *Journal of Guidance, Control, and Dynamics*, Vol. 20, No. 1, 1997, pp. 143–149. doi:10.2514/2.4008
- [19] Lu, P., and Hanson, J., "Entry Guidance for the X-33 Vehicle," *Journal of Spacecraft and Rockets*, Vol. 35, No. 3, 1998, pp. 342–349. doi:10.2514/2.3332
- [20] Saraf, A., Leavitt, J. A., Chen, D. T., and Mease, K. D., "Design and Evaluation of an Acceleration Guidance Algorithm for Entry," *Journal of Spacecraft and Rockets*, Vol. 41, No. 6, 2004, pp. 986–996. doi:10.2514/1.11015
- [21] Shen, Z., and Lu, P., "On-Board Generation of Three-Dimensional Constrained Entry Trajectories," *Journal of Guidance, Control, and Dynamics*, Vol. 26, No. 1, 2003, pp. 111–121. doi:10.2514/2.5021
- [22] Shen, Z., and Lu, P., "On-Board Entry Trajectory Planning for Sub-Orbital Flight," *Acta Astronautica*, Vol. 56, No. 6, 2005, pp. 573–591. doi:10.1016/j.actaastro.2004.10.005
- [23] Shen, Z., and Lu, P., "Dynamic Lateral Guidance Logic," *Journal of Guidance, Control, and Dynamics*, Vol. 27, No. 6, 2004, pp. 949–959. doi:10.2514/1.8008
- [24] Zimmerman, C., Dukeman, G., and Hanson, J., "Automated Method to Compute Orbital Reentry Trajectories with Heating Constraints," *Journal of Guidance, Control, and Dynamics*, Vol. 26, No. 4, 2003, pp. 523–529. doi:10.2514/2.5096
- [25] Hanson, J. M., and Jones, R. E., "Test Results for Entry Guidance Methods for Space Vehicles," *Journal of Guidance, Control, and Dynamics*, Vol. 27, No. 6, 2004, pp. 960–966. doi:10.2514/1.10886
- [26] Gamble, J. D., Cerimele, C. J., Moore, T. E., and Higgins, J., "Atmospheric Guidance Concepts for an Aeroassisted Flight Experiment," *Journal of Astronautical Sciences*, Vol. 36, No. 1, 1988, pp. 45–71.
- [27] Braun, R. D., and Powell, R. W., "Predictor-Corrector Guidance Algorithm for Use in High-Energy Aerobraking System Studies," *Journal of Guidance, Control, and Dynamics*, Vol. 15, No. 3, 1992, pp. 672–678. doi:10.2514/3.20890
- [28] Fuhry, D. P., "Adaptive Atmospheric Reentry Guidance for the Kistler K-1 Orbital Vehicle," AIAA Paper 1999-4211, Aug. 1999.
- [29] Kaluzhskikh, Y. N., and Sikharulidze, Y. G., "Control Algorithm for Reentry of a Rescue Space Vehicle into the Earth's Atmosphere," *Cosmic Research*, Vol. 38, No. 3, 2000, pp. 262–269.
- [30] Lu, P., "Predictor-Corrector Entry Guidance for Low Lifting Vehicles," *Journal of Guidance, Control, and Dynamics*, Vol. 31, No. 4, 2008, pp. 1067–1075. doi:10.2514/1.32055
- [31] Xue, S., and Lu, P., "Constrained Predictor-Corrector Entry Guidance," *Journal of Guidance, Control, and Dynamics*, Vol. 33, No. 4, 2010, pp. 1273–1280. doi:10.2514/1.49557
- [32] Lu, P., Forbes, S., and Baldwin, M., "Gliding Guidance of High L/D Hypersonic Vehicles," AIAA Paper 2013-4648, Aug. 2013.
- [33] Cruciani, I., Divitiis, N. D., Matteis, G. D., and Filippone, E., "Autonomous Guidance for a Sub-Orbital Re-Entry Vehicle," International Astronautical Federation Paper IAC-03-A.7.06, Oct. 2003.
- [34] Nocedal, J., and Wright, S. J., *Numerical Optimization*, 2nd ed., Springer-Verlag, New York, 2006, Chap. 11.
- [35] Phillips, T. H., "A Common Aero Vehicle (CAV) Model, Description, and Employment Guide," Schafer Corp. for Air Force Research Laboratory and Air Force Space Command, Jan. 2003.
- [36] Vinh, N. X., Busemann, A., and Culp, R. D., *Hypersonic and Planetary Entry Flight Mechanics*, Univ. of Michigan Press, Ann Arbor, MI, 1980, Chap. 7.
- [37] Yu, W., and Chen, W., "Guidance Scheme for Glide Range Maximization of a Hypersonic Vehicle," AIAA Paper 2011-6714, Aug. 2011.
- [38] Lu, P., and Vinh, N. X., "Minimax Optimal Control for Atmospheric Fly-Through Trajectories," *Journal of Optimization Theory and Applications*, Vol. 57, No. 1, 1988, pp. 41–57. doi:10.1007/BF00939328
- [39] Lu, P., and Shen, Z., "A Unifying Treatment to Control of Nonlinear Systems with Two Time Scales," *Journal of Guidance, Control, and Dynamics*, Vol. 25, No. 5, 2002, pp. 975–979. doi:10.2514/2.4972
- [40] Lu, P., "Nonlinear Systems with Control and State Constraints," *Optimal Control Applications and Methods*, Vol. 18, No. 5, 1997, pp. 313–326. doi:10.1002/(SICI)1099-1514(199709/10)18:5<313::AID-OCA605>3.3.CO;2-B